

Copyright
by
Mukul Bhattacharya
2018

**The Thesis Committee for Mukul Bhattacharya
certifies that this is the approved version of the following thesis:**

**On explaining GRB prompt spectrum with
photospheric emission model**

**APPROVED BY
SUPERVISING COMMITTEE:**

Pawan Kumar, Supervisor

Sonia Paban, Co-Supervisor

**On explaining GRB prompt spectrum with
photospheric emission model**

by

Mukul Bhattacharya

THESIS

Presented to the Faculty of the Graduate School of

The University of Texas at Austin

in Partial Fulfillment

of the Requirements

for the Degree of

MASTER OF ARTS

The University of Texas at Austin

May 2018

Dedicated to my parents.

Acknowledgments

Firstly, I would like to thank my advisor, Pawan Kumar, for giving me the opportunity to work in his group. Pawan was very patient throughout and always made sure that he is available to answer all my research questions. His ability to distill even the most complicated questions into the basic physics concepts is invaluable and has always encouraged me to encounter and solve all research problems in that manner. He always provided a very open environment for scientific discussions where we were motivated to think critically and develop our own insights. I would also like to thank my co-advisor, Sonia Paban. I am really grateful to her for agreeing to be my co-advisor and be a part of my qualifying examination committee, just a few months before the examination. She has always been very receptive to my queries and always made sure that she provides her valuable feedback. I would also thank Milos for generously providing all computational resources that were necessary for performing my Monte Carlo simulations.

I would like to sincerely thank my undergraduate research advisors from Indian Institute of Science, Bangalore: Banibrata Mukhopadhyay and Subroto Mukerjee. Their helpful advice and guidance helped me immensely during my graduate school applications. During the last three years, they have been a constant source of support and have always motivated me to keep

working harder even when I lost hope faced with seemingly endless sequence of journal, graduate school application and fellowship rejections. I truly owe a significant part of my success in the recent months to them, without their help I might not have made it through. I cannot thank Bani enough for his hospitality during my recent stay in IISc.

I would also like to thank former graduate student of Pawan, Rodolfo Santana, for extending his valuable support in understanding the Monte Carlo Radiation Transfer simulations of photospheric emission in GRBs. Wenbin Lu, Pawan's current graduate student, has been my scientific mentor ever since I met him about two and a half years ago. While he is the best researcher that I have ever come across with extensive knowledge about almost any topic in Astronomy, he is easily the most hard working and self-motivated individual that I know. Getting the opportunity to participate in group discussions and brainstorming sessions with Pawan and Wenbin together is undoubtedly the most enriching experience for a beginner like me trying to transition from Physics to Astronomy. I consider myself very lucky for being a part of a research group with two such extremely brilliant and hard-working individuals.

I would like to thank Benny (Tsz Ho) Tsang and Aaron Smith, my fellow graduate students in the Astronomy Theory group. They were always great to talk to and seek any advice from. I have learnt a lot about Astronomy and graduate school life from both of them. My Physics classmates: Avik Roy, Daniyar Saparov, Ryota Takaki and Jihang Zhu, were great to hangout with and talk about life in graduate school and academia in general. I would also

like to thank the following graduate students with whom I shared considerable time with in and outside UT: Aditya Aravind, Gaurav Chaudhary, Abhranil Das, Harish Potti, Ajesh Kumar, Ashish Gangshettiwar and Sajal Sen. To have them around always made my graduate school experience more enjoyable and less stressful. I would like to thank Astronomy graduate coordinators: Susy Graves and Sandra Catlett, Physics graduate advisor John Keto and graduate coordinator Matthew Ervin for always being there to help me with any paperwork and making it easier to navigate through graduate school.

Lastly, I would extend my gratitude to my parents for always believing in me, supporting and encouraging me in all my academic pursuits. They motivated me to take up research in basic sciences as a career and have always been there to help me out of difficult situations in graduate school. I owe a significant part of my achievements to them. I have been guilty of always being very busy and not giving them as much time as they deserve, but they have always been very understanding about it.

On explaining GRB prompt spectrum with photospheric emission model

Publication No. _____

Mukul Bhattacharya, M.A.

The University of Texas at Austin, 2018

Supervisors: Pawan Kumar
Sonia Paban

In this thesis, we present our work towards understanding the radiation mechanism of Gamma Ray Bursts (GRBs) during prompt emission phase. We study the spectra of photospheric emission from highly relativistic gamma-ray burst outflows using a Monte Carlo (MC) code. We consider the Comptonization of photons with a fast cooled synchrotron spectrum in a relativistic jet with realistic photon to electron number ratio $N_\gamma/N_e = 10^5$, using mono-energetic protons which interact with thermalised electrons through Coulomb interaction. The photons, electrons and protons are cooled adiabatically as the jet expands outwards. We find that the initial energy distribution of the protons and electrons do not have any appreciable effect on the photon peak energy $E_{\gamma,peak}$ and the power-law spectrum above $E_{\gamma,peak}$. The Coulomb interaction between the electrons and the protons does not affect the output photon spectrum significantly as the energy of the electrons is elevated only marginally.

$E_{\gamma,peak}$ and the spectral indices for the low and high energy power-law tails of the photon spectrum remain practically unchanged even with electron-proton coupling. Increasing the initial optical depth τ_{in} results in slightly shallower photon spectrum below $E_{\gamma,peak}$ and fewer photons at the high-energy tail, although $f_\nu \propto \nu^{-0.5}$ above $E_{\gamma,peak}$ and up to ~ 1 MeV, independent of τ_{in} . We find that $E_{\gamma,peak}$ determines the peak energy and the shape of the output photon spectrum. Lastly, we find that our simulation results are quite sensitive to N_γ/N_e , for $N_e = 3 \times 10^3$. For almost all our simulations, we obtain an output photon spectrum with power-law tail above $E_{\gamma,peak}$ extending up to ~ 1 MeV.

Table of Contents

Acknowledgments	v
Abstract	viii
List of Figures	xii
Chapter 1. Introduction	1
Chapter 2. Implementation of the photospheric code	8
2.1 Input parameters	8
2.2 Initialisation of electrons, protons and photons	12
2.2.1 Direction and energy of electrons and protons	12
2.2.2 Direction, energy and position of photons	13
2.3 Adiabatic cooling of electrons, protons and photons	13
2.4 Coulomb interaction	14
2.4.1 Electron-proton (e-p) interaction	15
2.4.2 Electron-electron (e-e) interaction	16
2.5 Main photospheric code	17
2.6 Photospheric code validation tests	19
Chapter 3. Monte Carlo simulation results	24
3.1 Effect of electron and proton initial energies	24
3.2 Effect of initial optical depth	26
3.3 Effect of seed photon energy	27
3.4 Evolution of electron and proton energies	30
3.5 Effect of photon to electron number ratio	31
3.6 Effect of geometrical broadening	33

Chapter 4. Discussion of results	35
4.1 Effect of simulation parameters on the output spectrum	35
4.2 Energy constraint for power-law above $E'_{\gamma,peak}$	38
4.3 Energy evolution for the photons, protons and electrons	39
4.3.1 Photons	39
4.3.2 Protons	40
4.3.3 Electrons	40
4.4 Equilibrium γ'_e of electrons	42
4.5 Effect of N_γ/N_e on simulation results	43
Chapter 5. Conclusions	45
Appendices	48
Appendix A. Initialization of photon energy	49
Appendix B. Electron-photon scattering probability	51
Appendix C. Pair production and annihilation	53
Bibliography	56
Vita	62

List of Figures

1.1	A GRB can result either from the merger of neutron stars or with the collapse of a massive star. From these events, a black hole with disk around it is formed which ejects a jet of material at relativistic velocities. Gamma rays are produced at relatively smaller distances from the central engine whereas longer wavelength radiation such as X-rays, visible light and radio waves are produced at much longer distances where the jet becomes optically very thin. Figure taken from Gehrels, Piro & Leonard: Scientific American, December 2002.	2
1.2	GRBs are isotropically distributed over space and do not tend to have any preferential position in the sky. They are extremely energetic events with energies, $E_{GRB} \sim L_{GRB} t_{GRB} \approx 10^{50} - 10^{53}$ erg, making them one of the most energetic events in the Universe since the Big Bang. Figure taken from G. Fishman et al., BATSE GRB Final Sky Map, June 2000.	4
1.3	There are two distinct classes of GRBs based on their observed duration: (a) short GRBs with duration $t_{GRB} < 2$ s are formed by the merger of a neutron star with another neutron star (NS-NS) or neutron star with a black hole (NS-BH). (b) long GRBs with duration $t_{GRB} > 2$ s are formed from the collapse of massive stars. Figure taken from Klenlin et al. 2014.	6
2.1	GRB prompt emission spectrum has a distinct power-law shape which is modelled by the Band function [1]. The observed low/high energy spectral index is $\alpha \sim 0/\beta \sim -1.2$ while the peak photon energy is $E_{\gamma,peak} \sim 300$ keV. The above picture demonstrates the excellent agreement of the modelled Band function parameters with observations from multiple telescopes. Figure is taken from NASA/IPAC Extragalactic Database. . .	9
2.2	Synchrotron seed photons are produced by fast cooled electrons at large optical depths $\tau_{in} \gtrsim 50$. These photons undergo many scatterings, especially at large optical depths to attain a Planck distribution. The electron thermalization timescale is very short and they exhibit a Maxwellian distribution with temperature determined by peak energy $\gamma_{e,in}$	11

2.3	Code validation tests. <i>Left Panel:</i> Obtaining equilibrium electron and photon distributions for $\Gamma = 300$, $k_B T'_{\gamma,in} = 1000$ eV, $N_\gamma/N_e = 2 \times 10^6 / 2 \times 10^4$ and no adiabatic cooling for Maxwellian electrons with constant $\gamma'_{e,in} = 1.001$ and $\tau_{in} = 100, 300$ and 500 . The low-energy spectral indices are: $\alpha_{\tau_{in}} = 2.17 \pm 0.07, 2.50 \pm 0.08$ and 2.85 ± 0.20 for $\tau_{in} = 100, 300$ and 500 respectively. The error bars for few selected points (yellow dots) on the photon distribution are shown - most of the error bars are too small to see except for low energies where the Poisson fluctuations are considerable due to small photon numbers. The electron and photon peak energies do not coincide but differ by a factor of ~ 2 as their average energies are different by a factor of 2 for the same equilibrium temperature. <i>Right Panel:</i> Comparison of our simulation results (dashed lines) with those from Figure 1 of [2] (solid lines) for Wien photons with $T_{\gamma,in} = 10^6$ K, $N_\gamma/N_e = 10^3$ and no adiabatic cooling for Maxwell-Juttner electrons with $T_{e,in} = 6.5 \times 10^9$ K and $\tau_{in} = 5$ and 75	21
2.4	Comparison of $N_\gamma = 10^8, N_e = 10^3, N_p = 10^3$ simulation results with $N_\gamma = 4 \times 10^8, N_e = 4 \times 10^3, N_p = 4 \times 10^3$ simulation results for photons with seed spectrum given by Equation 2.1, $\gamma'_{e,in} = 100$ and $\gamma'_{p,in} = 1.5$ for $\tau_{in} = 2$. <i>Left Panel:</i> When only adiabatic cooling is considered. <i>Right Panel:</i> When both adiabatic cooling and Coulomb interaction (e-p and e-e) are considered.	22
3.1	Simulation results for photons with seed spectrum given by Equation 2.1, $\tau_{in} = 4$ and with Coulomb interaction (both e-p and e-e). <i>Top-Left Panel:</i> For $\gamma'_{p,in} = 1.5$ and $\gamma'_{e,in} = 25, 50, 75$ and 100 . <i>Top-Right Panel:</i> For $\gamma'_{p,in} = 2$ and $\gamma'_{e,in} = 25, 50, 75$ and 100 . <i>Bottom-Left Panel:</i> For $\gamma'_{p,in} = 5$ and $\gamma'_{e,in} = 25, 50, 75$ and 100 . <i>Bottom-Right Panel:</i> For $\gamma'_{p,in} = 10$ and $\gamma'_{e,in} = 25, 50, 75$ and 100	25
3.2	Comparison of simulation results for photons with seed spectrum given by Equation 2.1, with Coulomb interaction (e-p and e-e) and different $\tau_{in} = 2, 4, 8$ and 16 . <i>Left Panel:</i> For $\gamma'_{p,in} = 1.5$ and $\gamma'_{e,in} = 100$. <i>Right Panel:</i> For $\gamma'_{p,in} = 5$ and $\gamma'_{e,in} = 50$. . .	26
3.3	Comparison of simulation results for photons with seed spectrum given by Equation 2.1 and different $E'_{\gamma,peak} = h\nu'_{sa} = 0.2$ eV, 2 eV and 20 eV, for $\tau_{in} = 4$ and with Coulomb interaction (e-p and e-e). <i>Left Panel:</i> For $\gamma'_{p,in} = 1.5$ and $\gamma'_{e,in} = 100$. <i>Right Panel:</i> For $\gamma'_{p,in} = 10$ and $\gamma'_{e,in} = 25$	28

3.4	Evolution of γ'_e for 3 electrons and γ'_p for 3 protons, for photons with seed spectrum given by Equation 2.1 and $\tau_{in} = 8$, $\gamma'_{e,in} = 75$ and $\gamma'_{p,in} = 2$. <i>Top-Left and Top-Right Panels:</i> Without e-p and e-e interactions. <i>Middle-Left and Middle-Right Panels:</i> With e-p and without e-e interaction. <i>Bottom-Left and Bottom-Right Panels:</i> With e-p and e-e interactions.	29
3.5	Comparison of simulation results for photons with seed spectrum given by Equation 2.1, $\tau_{in} = 2$ and with Coulomb interaction (e-p and e-e) for different $N_\gamma/N_e = 3 \times 10^6/3 \times 10^3, 3 \times 10^7/3 \times 10^3$ and $3 \times 10^8/3 \times 10^3$. <i>Left Panel:</i> For $\gamma'_{p,in} = 1.5$ and $\gamma'_{e,in} = 100$. <i>Right Panel:</i> For $\gamma'_{p,in} = 5$ and $\gamma'_{e,in} = 50$	31
3.6	Broadening of seed photon spectrum for large $\tau_{in} = 2, 4$ and 8 , with Coulomb interaction (e-p and e-e), $\gamma'_{e,in} = 100$, $\gamma'_{p,in} = 1.5$, $N_\gamma = 10^8$ and $N_e = 10^3$. <i>Left Panel:</i> For monoenergetic photon seed spectrum with $E'_{\gamma,peak} = 20$ eV. <i>Right Panel:</i> For blackbody (BB) photon seed spectrum with $E'_{\gamma,peak} = 20$ eV. .	32

Chapter 1

Introduction

The radiation mechanism responsible for the prompt emission of Gamma-Ray Bursts (GRBs) is still not very well understood. The observed spectra is generally modelled using the Band function [1], which is a smoothly connected broken power-law with observed peak energy $E_p \sim 300$ keV and non-thermal power-laws below and above the peak (in some cases up to \sim GeV energies) [2, 3, 4]. The two most widely explored models to explain the GRB spectrum are the internal dissipation model and the photospheric model [5, 6, 7].

In the internal dissipation model, the energy is dissipated either by internal shocks [5] or by magnetic reconnection in a Poynting dominated jet [8]. The prompt radiation is due to the synchrotron emission from non-thermal electrons gyrating in a shock-generated magnetic field [9, 10, 11]. This model suffers from low radiation efficiency because only the kinetic energy associated with the differential motion of the shells can be dissipated and not the kinetic energy associated with the bulk motion of the jet [12, 13, 14, 15, 16]. However, the observations confirm high efficiencies up to few tens of percent [17]. Moreover, synchrotron emission cannot explain hard GRB spectra at low energies [18, 19] and the spectrum is directly related to the radiation mechanism

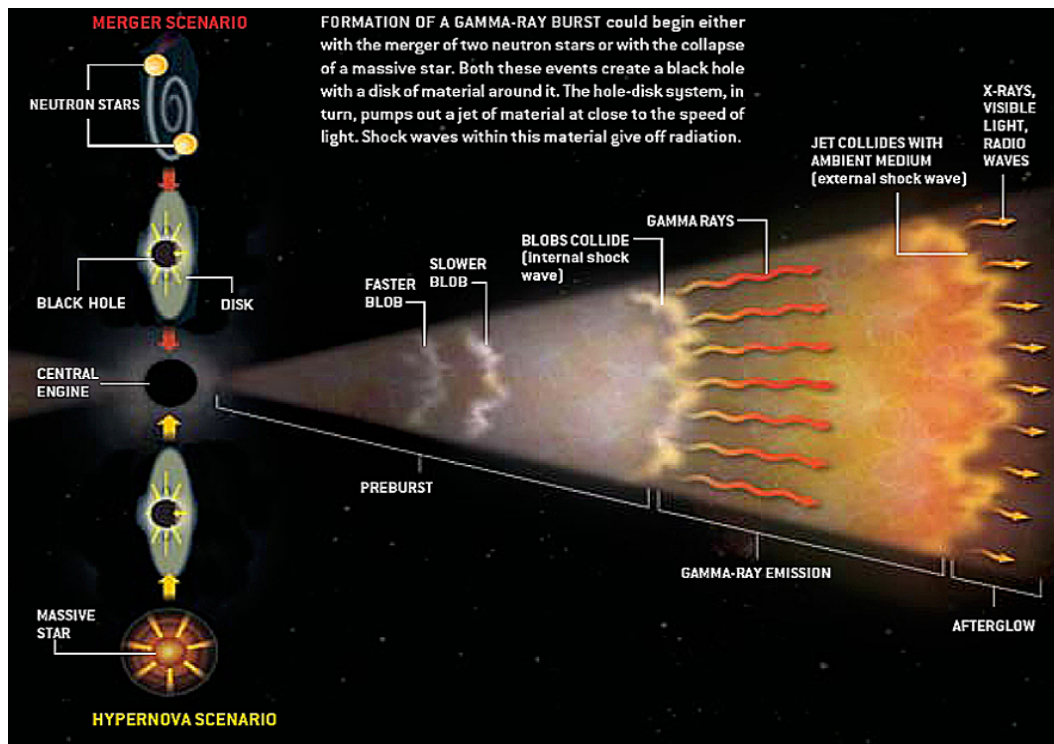


Figure 1.1: A GRB can result either from the merger of neutron stars or with the collapse of a massive star. From these events, a black hole with disk around it is formed which ejects a jet of material at relativistic velocities. Gamma rays are produced at relatively smaller distances from the central engine whereas longer wavelength radiation such as X-rays, visible light and radio waves are produced at much longer distances where the jet becomes optically very thin. Figure taken from Gehrels, Piro & Leonard: Scientific American, December 2002.

involved rather than interaction with baryons and leptons in the jet.

Owing to these shortcomings of the internal dissipation model, many researchers have recently focussed on the photospheric emission model [20, 21, 22, 23, 2, 24]. Unlike the internal dissipation model, the photospheric model can explain the observed high radiation efficiencies. The shape of the spectrum is determined by the interaction of photons with matter in the jet, which is through Compton scattering, and hence should be independent of the emission mechanism. There have been many successful attempts to explain the high-frequency non-thermal tails using sub-photospheric dissipation [25, 26, 22, 27, 23, 2, 24], however non-thermal tails at low energies still cannot be obtained [28, 2].

GRBs can be generated from two different mechanisms each of which create a black hole with a disk around it: (a) merger of two neutron stars with each other, or (b) collapse of a massive star onto itself. The material from the black hole-disk system is ejected out at highly relativistic velocities and gives rise to the observed radiation. Figure 1.1 shows the general structure of these jets and their propagation in space. Initially, the jet carries the bulk of the kinetic energy which is dissipated into the thermal energy of the electrons and protons by a variety of mechanisms such as internal shocks, magnetic reconnection and neutron-proton collisions. The electrons then transfer their energy to the photons through Comptonization which is radiated away as gamma rays. The electrons are maintained at sub-relativistic energies by continuous heating from collisions with protons as well as episodic sub-photospheric dissipation

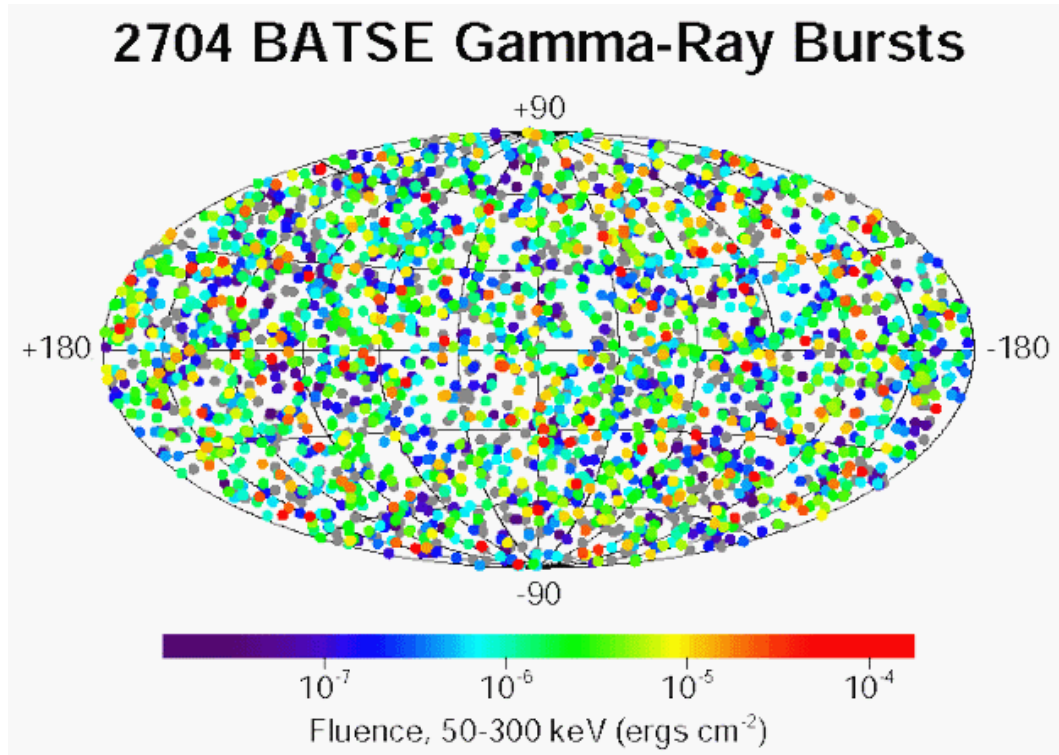


Figure 1.2: GRBs are isotropically distributed over space and do not tend to have any preferential position in the sky. They are extremely energetic events with energies, $E_{GRB} \sim L_{GRB} t_{GRB} \approx 10^{50} - 10^{53}$ erg, making them one of the most energetic events in the Universe since the Big Bang. Figure taken from G. Fishman et al., BATSE GRB Final Sky Map, June 2000.

events. As the jet expands outwards, the electrons, protons and photons cool down significantly due to adiabatic energy loss.

As shown in Figure 1.2, these highly energetic events are isotropically distributed all over the sky. Their luminosities are extremely large $\sim 10^{51} - 10^{52}$ erg/s which makes them one of the most energetic explosions in the Universe since the Big Bang. GRBs are classified into two separate groups based on their observed duration t_{GRB} , as shown in Figure 1.3. Bursts with $t_{GRB} < 2$ s result from the merger of a neutron star with another neutron star (NS-NS) or another black hole (NS-BH). Whereas bursts with $t_{GRB} > 2$ s are generated from the collapse of massive stars onto themselves.

In this thesis, we study the Comptonisation of seed photons produced by synchrotron emission of fast cooling electrons below the photosphere [29, 30]. The electrons and protons are accelerated to relativistic energies by a dissipation mechanism such as internal shocks [22, 31, 32] or magnetic reconnection [33, 26, 34] at an optical depth of a few or larger. The choice of synchrotron spectrum over thermal spectrum for photons is justified as there are not enough scatterings at relatively small optical depths $\tau \approx 10$ to thermalise the photon spectrum [35]. Most of the energy in the jet is carried by the protons because of their large mass and the average energy of the electrons is assumed to be much larger as compared to the average energy of the photons. We consider sub-photospheric heating of electrons which occurs as a result of continuous injection of energy from the protons through the Coulomb interaction and is more physically motivated than episodic injection of energy

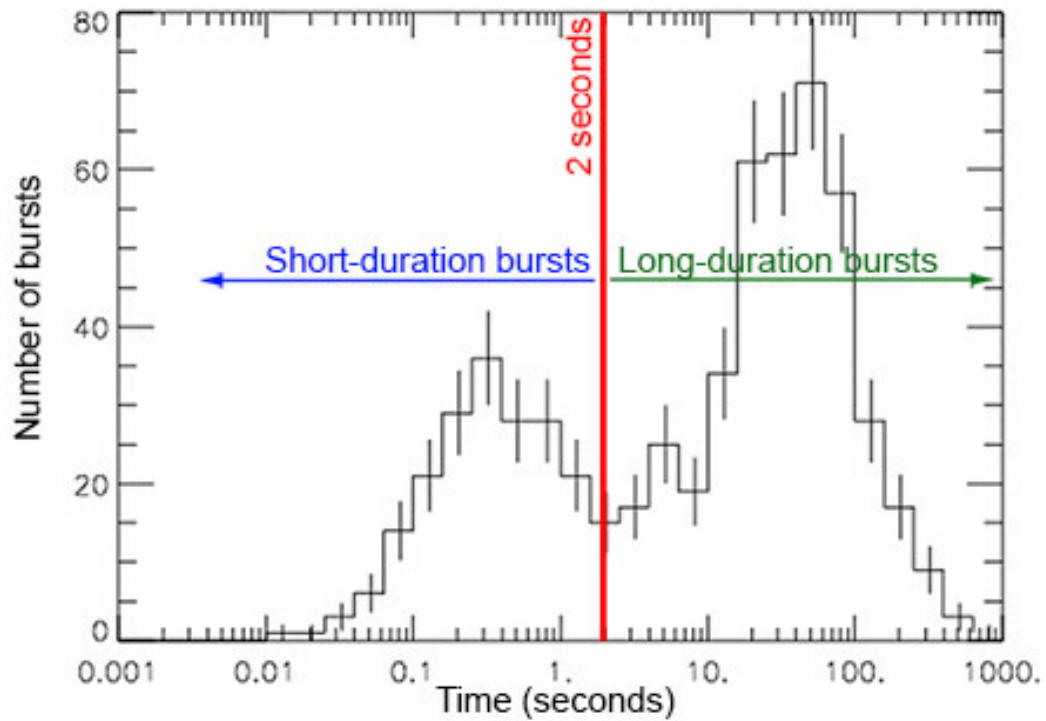


Figure 1.3: There are two distinct classes of GRBs based on their observed duration: (a) short GRBs with duration $t_{GRB} < 2$ s are formed by the merger of a neutron star with another neutron star (NS-NS) or neutron star with a black hole (NS-BH). (b) long GRBs with duration $t_{GRB} > 2$ s are formed from the collapse of massive stars. Figure taken from Klenlin et al. 2014.

[26, 25, 22, 24]. Photons undergo multiple scatterings with the electrons and gain energy until the outflow becomes optically thin and the photons escape the photosphere. Unlike many previous photospheric MC simulations [22, 2], we also include adiabatic cooling of electrons, protons and photons due to the expansion of the relativistic jet [24].

Almost all photospheric MC simulations performed previously used relatively small photon to electron ratio $N_\gamma/N_e \sim 10^1 - 10^4$ [22, 2], which leads to unrealistically low radiation efficiencies contradicting GRB observations [17, 24]. In this work, we use $N_\gamma/N_e = 10^5$ which gives radiative efficiency $\eta \sim 10\%$ (consistent with observations) in addition to incorporating electron heating in a more realistic way to determine if the high-energy GRB prompt emission spectral index can be reproduced using the photospheric emission model. For all our simulations, we use Maxwell-Boltzmann (MB) electrons and mono-energetic protons as the respective seed distributions.

This thesis is organized as follows. In Chapter 2, we describe the physics and implementation of our MC photospheric code. We present our simulation results in Chapter 3 and discuss the interpretation of these results in Chapter 4. Finally, we present our conclusions in Chapter 5.

Chapter 2

Implementation of the photospheric code

In this chapter, we describe the implementation of our MC code and give an overview of the basic physics included. We discuss how the energy and velocity distributions of the electrons, protons and photons are initialised and how they are affected by adiabatic cooling, Coulomb interaction and scattering events. The scattering events between the electrons and photons are performed one at a time in our MC code. Throughout this thesis, primed quantities are in the jet-comoving frame while unprimed quantities are in the lab frame.

2.1 Input parameters

Here we describe the input parameters used for our MC simulations.

- Isotropic equivalent luminosity of the jet, L : We consider $L = 10^{52}$ ergs/sec for all our simulations [36, 37].
- Bulk Lorentz factor of the jet, Γ : For all our simulations, we consider $\Gamma = 300$ [38, 39].
- Number of electrons in a simulation, N_e : Like in the previous photospheric simulations [22, 2, 24], we consider $N_e = 10^3$. In Figure 2.4, we

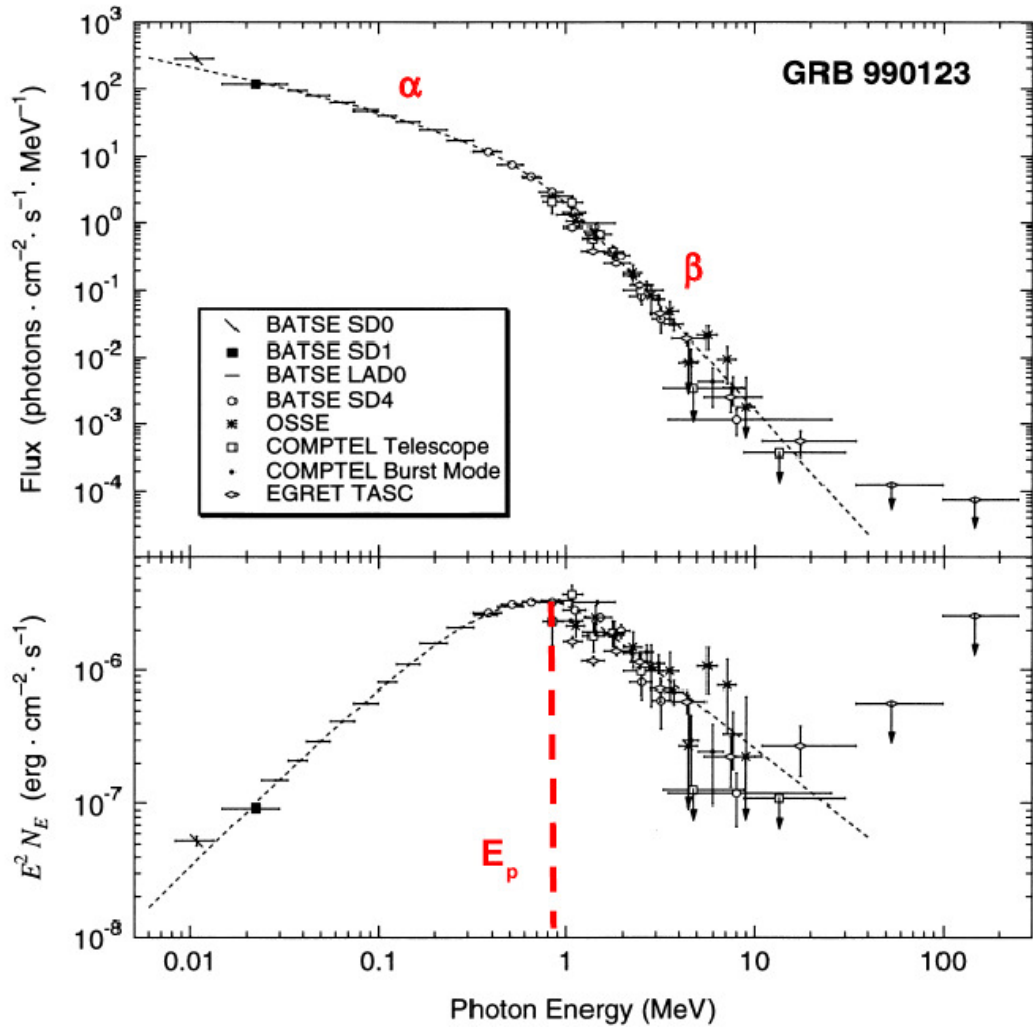


Figure 2.1: GRB prompt emission spectrum has a distinct power-law shape which is modelled by the Band function [1]. The observed low/high energy spectral index is $\alpha \sim 0/\beta \sim -1.2$ while the peak photon energy is $E_{\gamma,peak} \sim 300$ keV. The above picture demonstrates the excellent agreement of the modelled Band function parameters with observations from multiple telescopes. Figure is taken from NASA/IPAC Extragalactic Database.

show that it is enough to use 10^3 electrons for accurately simulating the GRB jet.

- Number of photons in a simulation, N_γ : We consider $N_\gamma = 10^8$ for our simulations [24]. This was done to ensure that $N_\gamma/N_e = 10^5$.
- Number of protons in a simulation, N_p : We consider $N_p = 10^3$ as $N_e = N_p$ due to charge neutrality of the jet.
- Number of photons collected for the output spectrum, $N_{\gamma,\text{collect}}$: Like in the previous simulations [22, 24], we consider $N_{\gamma,\text{collect}} = N_\gamma/3$ as it gives us a time-averaged representation of the GRB spectrum by allowing for enough photon-electron scatterings to accurately represent the output spectrum.
- Initial optical depth, τ_{in} : The initial optical depth determines the distance from the central engine where all the electrons, photons and protons are injected. We consider $\tau_{in} = 2, 4, 8$ and 16 in this work.
- Seed photon spectrum : We consider the synchrotron spectrum for fast cooling electrons where the energy distribution is given by smoothly connected power-laws [30, 6]:

$$f_\nu = \begin{cases} \left(\frac{\nu_{ac}}{\nu_{sa}}\right)^{11/8} \left(\frac{\nu}{\nu_{ac}}\right)^2, & \nu_l < \nu < \nu_{ac} \\ \left(\frac{\nu}{\nu_{sa}}\right)^{11/8}, & \nu_{ac} < \nu < \nu_{sa} \\ \left(\frac{\nu}{\nu_{sa}}\right)^{-1/2}, & \nu_{sa} < \nu < \nu_m \\ \left(\frac{\nu_m}{\nu_{sa}}\right)^{-1/2} \left(\frac{\nu}{\nu_m}\right)^{-p/2}, & \nu_m < \nu < \nu_u \end{cases} \quad (2.1)$$

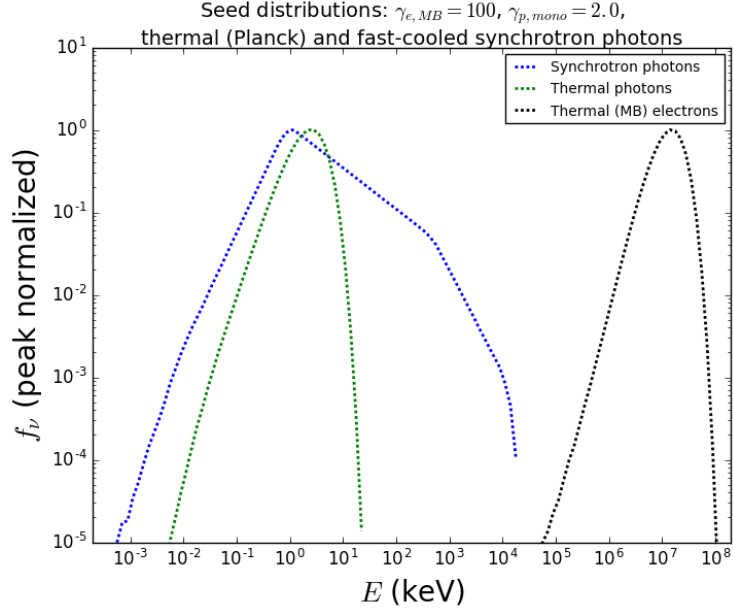


Figure 2.2: Synchrotron seed photons are produced by fast cooled electrons at large optical depths $\tau_{in} \gtrsim 50$. These photons undergo many scatterings, especially at large optical depths to attain a Planck distribution. The electron thermalization timescale is very short and they exhibit a Maxwellian distribution with temperature determined by peak energy $\gamma_{e,in}$.

where f_ν is the flux per unit frequency in the lab frame. Throughout this thesis we consider, $h\nu'_l = 3 \times 10^{-9}$ eV, $h\nu'_{ac} = 2 \times 10^{-2}$ eV, $h\nu'_{sa} = 2$ eV, $h\nu'_m = 1$ keV and $h\nu'_u = 30$ keV, which is justified by the choice of our parameters and the typical values of other parameters: $\epsilon_B = 0.1$, $\epsilon_e = 0.1$, $N = 10^2$ and $T = 10$ s [30]. f_ν is peak normalised and the high energy spectral index $p = 2.5$ [7].

- Electron distribution : We consider Maxwell-Boltzmann (MB) distribution of electrons with the initial $\gamma'_{e,in}$ as the input parameter. For our

simulations, $\gamma'_{e,in} = 25, 50, 75$ and 100 .

- Proton distribution : For our simulations, we consider mono-energetic distribution of protons with the initial $\gamma'_{p,in}$ as the input parameter. We perform the simulations using $\gamma'_{p,in} = 1.5, 2, 5$ and 10 .

2.2 Initialisation of electrons, protons and photons

At the beginning of our photospheric MC code, we initialise the directions and energies of all the electrons, protons and photons.

2.2.1 Direction and energy of electrons and protons

The initial directions of the velocities of N_e electrons and N_p protons are chosen randomly in the comoving frame of the jet (see Appendix B1 of [24]). For the initial energies of the electrons, γ'_e is chosen from the relativistic MB distribution corresponding to temperature $T'_{e,in}$ which is given by (see Appendix B2.1 of [24]),

$$k_B T'_{e,in} = (\gamma'_{ad,e,in} - 1)(\gamma'_{e,in} - 1)m_e c^2 \quad (2.2)$$

where, the electron adiabatic index $\gamma'_{ad,e,in} \approx (4\gamma'_{e,in} + 1)/(3\gamma'_{e,in})$. For the mono-energetic protons, $\gamma'_p = \gamma'_{p,in}$. We assume that initially all the N_e electrons and N_p protons are distributed uniformly in the comoving frame of the jet.

2.2.2 Direction, energy and position of photons

The initial directions of the velocities of N_γ photons are chosen randomly in the comoving frame of the jet (see Appendix C1 of [24]). The initial energies of the photons in the comoving frame of the jet is chosen from the synchrotron radiation distribution of fast cooling electrons as given in Equation 2.1 (see Appendix A for algorithm).

The position of the N_γ photons are assigned randomly and they are uniformly distributed within a cone with solid angle $1/\Gamma$ pointing towards the observer. The initial distance from the central engine (in the lab frame) where the photons are injected is given by

$$R_{in} = \frac{L\sigma_T}{8\pi m_p c^3 \beta \Gamma^3 \tau_{in}} \quad (2.3)$$

where $\beta = \sqrt{1 - (1/\Gamma^2)}$ and σ_T is the Thomson cross section.

2.3 Adiabatic cooling of electrons, protons and photons

The energies of the electrons, protons and photons decreases as the jet expands outward, due to adiabatic cooling. Due to the adiabatic cooling, the energy of the electrons [protons] decreases by a factor $R^{-2(\gamma'_{ad,e}-1)}$ [$R^{-2(\gamma'_{ad,p}-1)}$] where $\gamma'_{ad,e} \approx (4\gamma'_e + 1)/(3\gamma'_e)$ [$\gamma'_{ad,p} \approx (4\gamma'_p + 1)/(3\gamma'_p)$] is the adiabatic index of the electron [proton] and R is the radial distance the jet has travelled from the central engine. For the photons, the drop in energy is by a factor $R^{-2/3}$. These expressions are valid because the electron density n'_e drops by a factor R^2 as the relativistic outflow expands outward and the radial width of the jet

remains unchanged. After each scattering event, the energies of the electrons, protons and photons are modified due to adiabatic cooling as

$$\frac{\gamma'_{e,f} - 1}{\gamma'_{e,i} - 1} = \left(\frac{R_{in} + (t_\gamma + \Delta t_\gamma)\beta c}{R_{in} + t_e\beta c} \right)^{-2(\gamma'_{ad,e,i}-1)} \quad (2.4)$$

$$\frac{\gamma'_{p,f} - 1}{\gamma'_{p,i} - 1} = \left(\frac{R_{in} + (t_\gamma + \Delta t_\gamma)\beta c}{R_{in} + t_e\beta c} \right)^{-2(\gamma'_{ad,p,i}-1)} \quad (2.5)$$

$$\frac{E'_{\gamma,f}}{E'_{\gamma,i}} = \left(\frac{R_{in} + (t_\gamma + \Delta t_\gamma)\beta c}{R_{in} + t_\gamma\beta c} \right)^{-2/3} \quad (2.6)$$

where R_{in} is given by Equation 2.3. The subscripts i and f are used to denote the energies before and after the photon has travelled a distance s' in the comoving frame of the jet. The total time elapsed in the lab frame for the photon and electron (which undergo scattering) is given by t_γ and t_e , respectively. The time needed by the photon to travel a distance s' in the lab frame is given by Δt_γ (see Appendix C3 of [24] for Lorentz transformation). The proton is considered to be moving with the electron and hence can be represented by the same time t_e as it is practically unaffected by the photon-electron scattering event. After the photon travels a distance s' , the electron and the photon reach the same final radial position where they interact by IC/Compton scattering.

2.4 Coulomb interaction

In addition to adiabatic cooling, the energies of the electrons and the protons are also affected by the Coulomb interaction between them. As the protons have much larger energies as compared to the electrons, electrons

are always heated due to the energy transfer from the protons. Moreover, the electrons exchange energy between themselves and attain MB distribution after reaching equilibrium. Below we discuss how the electron and proton energies are affected due to these interactions.

2.4.1 Electron-proton (e-p) interaction

The timescale for Coulomb cooling of protons in the jet-comoving frame is,

$$t'_{p,Coul} = \frac{(\gamma'_p - 1)m_p c^2 (8.3 \times 10^{-15} T_e'^{3/2} + \beta_p'^3)}{5 \times 10^{-19} n'_e \beta_p'^2} \quad (2.7)$$

where n'_e is the electron density in the jet-comoving frame, T'_e is the temperature of the electrons in the jet-comoving frame and β'_p is the speed of the protons divided by the speed of light. The electron density n'_e is given by

$$n'_e = \frac{L}{4\pi(R_{in} + t_e \beta c)^2 m_p c^3 \Gamma^2} \quad (2.8)$$

The energies of the protons and electrons are modified due to Coulomb interaction after each scattering event. The expressions used to update the γ'_e of an electron and γ'_p of a proton due to Coulomb interaction are

$$\gamma'_{e,f} = \gamma'_{e,i} + \frac{5 \times 10^{-19} n'_e}{\Gamma m_e c^2} \frac{\beta_{p,i,avg}^2 (t_\gamma + \Delta t_\gamma - t_e)}{(8.3 \times 10^{-15} T_{e,i,avg}'^{3/2} + \beta_{p,i,avg}'^3)} \quad (2.9)$$

$$\gamma'_{p,f} = \gamma'_{p,i} - \frac{5 \times 10^{-19} n'_e}{\Gamma m_p c^2} \frac{\beta_{p,i,avg}^2 (t_\gamma + \Delta t_\gamma - t_e)}{(8.3 \times 10^{-15} T_{e,i,avg}'^{3/2} + \beta_{p,i,avg}'^3)} \quad (2.10)$$

As before, the subscripts i and f are used to denote the energies before and after the photon travels by a distance s' in the jet-comoving frame. The factor

of $1/\Gamma$ is included to transform the time from the lab frame to the jet-comoving frame. As the electrons experience Coulomb heating due to the average proton distribution around them and vice-versa, we include averaged quantities $\beta'_{p,i,avg}$ and $T'_{e,i,avg}$ which denote the speed of protons averaged over N_p protons in the jet-comoving frame divided by the speed of light and the temperature of electrons corresponding to $\gamma'_{e,i}$ averaged over N_e electrons in the jet-comoving frame (see Equation 2.2), respectively. Thus, after each scattering event, the electrons gain some energy from the protons which is determined by their respective energy distributions.

2.4.2 Electron-electron (e-e) interaction

In addition to interacting with the protons, the electrons also exchange energy between themselves. The energy distribution of the electrons at thermal equilibrium is given by MB distribution with the peak temperature $T'_{e,avg}$ determined by $\gamma'_{e,avg}$ (see Equation 2.2). As the nature of the interaction between the electrons is the same as that with the protons, the timescale for this interaction can be obtained just by replacing the proton parameters with the electron parameters in Equation 2.7,

$$t'_{e,Coul} = \frac{(\gamma'_{e,avg} - 1)m_e c^2}{5 \times 10^{-19} n'_e} \frac{(8.3 \times 10^{-15} T'^{3/2}_{e,avg} + \beta'^3_{e,avg})}{\beta'^2_{e,avg}} \quad (2.11)$$

where β'_e is the speed of electron in the jet-comoving frame divided by the speed of light and all the electron parameters are averaged over all N_e electrons. After each photon-electron scattering event, the average (over N_e electrons) total time elapsed in the lab frame is evaluated for the electrons, which is denoted

by $t_{e,avg}$. Whenever $t_{e,avg}$ exceeds any multiple of $t_{e,Coul} = \Gamma t'_{e,Coul}$, the electron distribution is re-initialised to a MB distribution with $T'_{e,avg}$ determined by $\gamma'_{e,avg}$ at that point of the simulation.

It should be noted that the electron distribution in between consecutive scattering events can deviate from Maxwellian for large values of N_γ/N_e (see Figure 3.5). In that case, the electron temperature $T'_{e,avg}$ evaluated from Equation 2.2 using $\gamma'_{e,avg}$ may not exactly correspond to that of a Maxwellian with the same energy. However, Equations 2.7 and 2.11 can still be used to model the Coulomb interactions fairly well as long as: (1) the quasi-Maxwellian distribution is unimodal with peak energy close to that of the approximated Maxwellian distribution, and (2) the timescale at which the electrons are re-initialised to Maxwellian distribution is comparable to the electron-photon scattering timescale. Both these conditions are satisfied for all our simulations and the electron distribution need not be updated after every scattering event which is computationally very expensive.

2.5 Main photospheric code

At the beginning of the simulation, the distance s' that each photon travels in the comoving frame of the jet before scattering an electron is drawn randomly using the formula $s' = -l'_{mfp} \ln(\alpha)$ [24]. Here, $l'_{mfp} = 1/(n'_e \sigma_T)$ is the mean free path of the photons in the jet-comoving frame and α is a uniformly distributed random number within 0 and 1. Once s' for all N_γ photons are drawn, the photons are propagated and their new positions are

Lorentz transformed to the lab frame (see Appendix C3 of [24]) and compared with the photospheric distance R_{ph} (R corresponding to $\tau = 1$ in Equation 2.3) to check if any photon escapes the photosphere without interacting with an electron. For the photons which escape the photosphere, the energies are Doppler boosted to the lab frame and are stored. All other photons are placed in a priority queue $(t_{\gamma,l}, l)$, where $t_{\gamma,l}$ denotes the total time elapsed in the lab frame for the photon with index l . The photon properties such as position, direction and energy can be accessed using the respective photon index l . The priority queue structure allows for the photon with the smallest $t_{\gamma,l}$ to get scattered first [24].

Next, we propagate the first photon in the priority queue using the corresponding s' . One of the N_p protons is chosen randomly while one of the N_e electrons is selected by sampling the electron-photon scattering probability distribution function (see Appendix B for algorithm) given by,

$$P_{scatt}(\beta'_e, \theta'_e) = \frac{1}{4\pi\beta_e'^2}(1 - \beta'_e \cos\theta'_e) \quad (2.12)$$

where, θ'_e is the angle between the electron and photon directions before the scattering event in the jet-comoving frame and β'_e is the speed of the electron in the jet-comoving frame divided by the speed of light.

Next, Equations 2.4 - 2.6 are used to update the energies after adiabatic cooling and Equations 2.9 - 2.10 are used to update the energies after Coulomb interaction. Once the energies are determined, the dimensionless photon energy in the electron rest frame z_i and the scattering cross-section $\sigma(z'_i)$ are

calculated (see Appendix D of [24]). A uniformly distributed random number $0 \leq \alpha_s \leq 1$ is drawn and is compared with the scattering probability $\sigma(z'_i)/\sigma_T$ to determine whether the electron-photon scattering event actually happens. If $\alpha_s \leq \sigma(z'_i)/\sigma_T$ is satisfied, the scattering event takes place and the direction and energy of the photon is updated along with the direction and energy of the electron (see Appendices D and E of [24]).

Finally, irrespective of whether the photon is scattered or not, a new s' is drawn at its current location and the photon is propagated as was done at the beginning of the simulation. The distance travelled by the photon is Lorentz transformed to the lab frame and whether the current location of the photon R exceeds R_{ph} is checked. If $R \geq R_{ph}$, the energy of the photon is Doppler boosted to the lab frame and is stored. Else, the photon is again placed in the priority queue with the updated total elapsed time in the lab frame $t_{\gamma,l}$ and the whole process is repeated until $N_{\gamma,collect}$ photons escape the photosphere.

2.6 Photospheric code validation tests

We first try to reproduce the equilibrium distributions for electrons and photons undergoing Compton scatterings to check the validity of our simulations. In the left panel of Figure 2.3, we present the results of simulations in which Maxwellian electrons are held fixed at energy $\gamma'_{e,in} = 1.001$ while they scatter Blackbody photons with $k_B T'_{\gamma,in} = 1000$ eV for $N_\gamma/N_e = 10^2$ and $\Gamma = 300$. The electrons and the photons are not cooled due to adiabatic

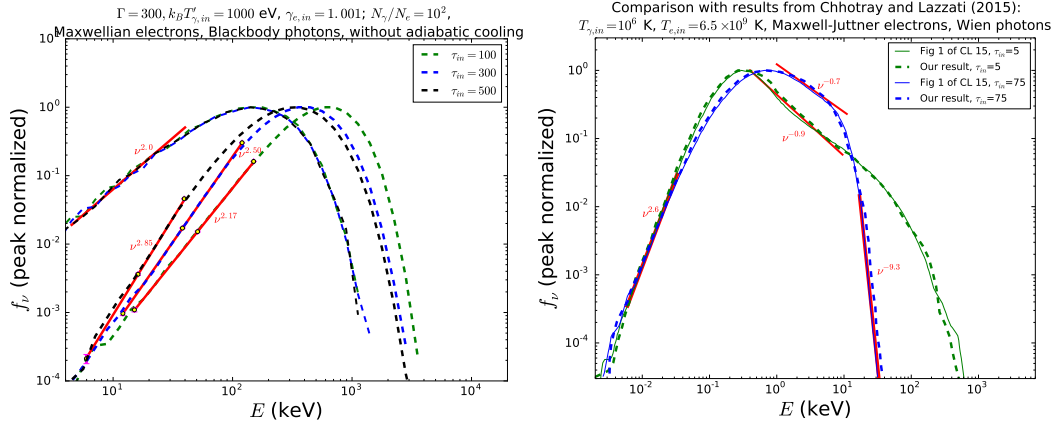


Figure 2.3: Code validation tests. *Left Panel:* Obtaining equilibrium electron and photon distributions for $\Gamma = 300$, $k_B T'_{\gamma,in} = 1000$ eV, $N_\gamma/N_e = 2 \times 10^6/2 \times 10^4$ and no adiabatic cooling for Maxwellian electrons with constant $\gamma'_{e,in} = 1.001$ and $\tau_{in} = 100, 300$ and 500 . The low-energy spectral indices are: $\alpha_{\tau_{in}} = 2.17 \pm 0.07$, 2.50 ± 0.08 and 2.85 ± 0.20 for $\tau_{in} = 100, 300$ and 500 respectively. The error bars for few selected points (yellow dots) on the photon distribution are shown - most of the error bars are too small to see except for low energies where the Poisson fluctuations are considerable due to small photon numbers. The electron and photon peak energies do not coincide but differ by a factor of ~ 2 as their average energies are different by a factor of 2 for the same equilibrium temperature. *Right Panel:* Comparison of our simulation results (dashed lines) with those from Figure 1 of [2] (solid lines) for Wien photons with $T_{\gamma,in} = 10^6$ K, $N_\gamma/N_e = 10^3$ and no adiabatic cooling for Maxwell-Juttner electrons with $T_{e,in} = 6.5 \times 10^9$ K and $\tau_{in} = 5$ and 75 .

expansion of the jet as the initial optical depth is varied, $\tau_{in} = 100, 300$ and 500 . For photons interacting with electrons kept at a constant temperature bath, the equilibrium distribution at large τ_{in} approaches Bose-Einstein distribution with a non-zero chemical potential while the electrons attain Maxwell-Boltzmann distribution.

We find that the equilibrium distribution (within uncertainty) for pho-

tons ($f_\nu \propto \nu^3$ at low energies and $f_\nu \propto e^{-\nu}$ at high energies) and electrons ($f_\nu \propto \nu^2$ at low energies and $f_\nu \propto e^{-\nu}$ at high energies) is obtained close to $\tau_{in} \sim 500$. It should be noted that the spectral indices obtained from the power-law fits in the left panel of Figure 2.3 (and the rest of the figures in this thesis) have statistical uncertainties due to the non-zero energy bin width, $\Delta E_{bw} = 1$ eV, and the relatively small number of photons at low energies (for $N_\gamma = 10^8$) in our simulation. However, these uncertainties are typically very small for the parameters that we consider and can be ignored.

In the right panel of Figure 2.3, we compare our simulation results with that of Figure 1 of [2] for the same input parameters: Wien photons with $T_{\gamma,in} = 10^6$ K, $N_\gamma/N_e = 10^3$ and no adiabatic cooling for Maxwell-Jüttner electrons with $T_{e,in} = 6.5 \times 10^9$ K and $\tau_{in} = 5$ and 75. We find that there is good agreement of our results with [2] for both the simulations which demonstrates that our photospheric code is working properly.

We then check whether $N_e = 10^3$, $N_p = 10^3$ and $N_\gamma = 10^8$ are appropriate choices for representing the electron, proton and photon distributions in the relativistic jet. MC photospheric simulations have been performed previously with $N_e = 10^3$ [22, 2], but smaller $N_\gamma/N_e \sim 10^1 - 10^4$ were considered for those simulations. Simulations have also been performed with thermal photons as the seed spectrum to show that $N_e = 10^3$ is enough to represent the electron distribution for $N_\gamma/N_e = 10^5$ [24], although e-p and e-e interactions were neglected in those simulations. We perform simulations with $N_\gamma = 10^8$, $N_e = 10^3$ and $N_p = 10^3$ and compare them with $N_\gamma = 4 \times 10^8$, $N_e = 4 \times 10^3$

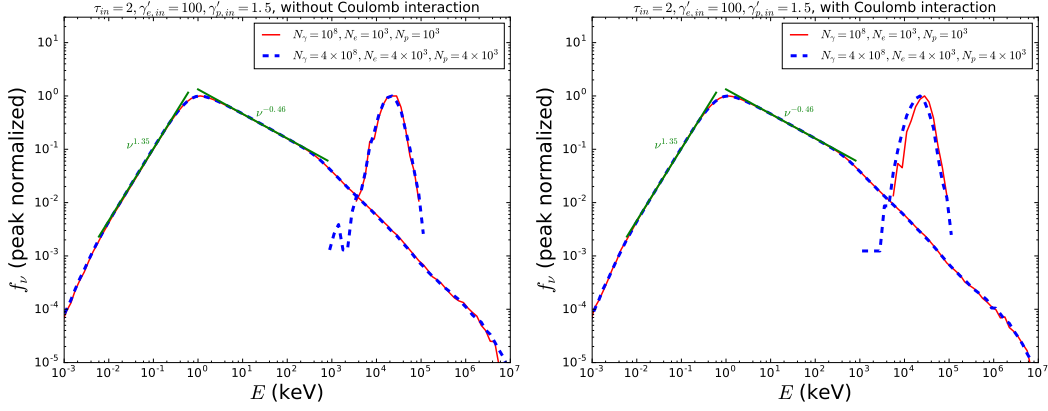


Figure 2.4: Comparison of $N_\gamma = 10^8, N_e = 10^3, N_p = 10^3$ simulation results with $N_\gamma = 4 \times 10^8, N_e = 4 \times 10^3, N_p = 4 \times 10^3$ simulation results for photons with seed spectrum given by Equation 2.1, $\gamma'_{e,in} = 100$ and $\gamma'_{p,in} = 1.5$ for $\tau_{in} = 2$. *Left Panel:* When only adiabatic cooling is considered. *Right Panel:* When both adiabatic cooling and Coulomb interaction (e-p and e-e) are considered.

and $N_p = 4 \times 10^3$ in Figure 2.4. For both panels, $\tau_{in} = 2$, $\gamma'_{e,in} = 100$ and $\gamma'_{p,in} = 1.5$ are considered and the seed photon distribution is given by Equation 2.1. The left panel shows simulations performed without considering Coulomb interactions whereas the right panel shows simulations where both e-p and e-e Coulomb interactions were considered. The very good agreement between the simulation results suggests that $N_e = N_p = 10^3$ is enough for accurately representing relativistic jets for $N_\gamma/N_e = 10^5$.

Chapter 3

Monte Carlo simulation results

In this chapter, we present the results of our photospheric MC simulations. In all the figures, the photon energy spectrum and the electron kinetic energy spectrum is in the lab frame (Doppler boosted from the jet-comoving frame by multiplying with Γ) at the end of each simulation. Unless stated otherwise, e-p and e-e interactions are considered for the simulations.

3.1 Effect of electron and proton initial energies

In Figure 3.1, we present the simulation results for different combinations of $\gamma'_{e,in}$ ($=25, 50, 75, 100$) and $\gamma'_{p,in}$ ($=1.5, 2, 5, 10$) at $\tau_{in} = 4$ when e-p and e-e interactions are considered. Comparing the different panels, we can see that $\gamma'_{p,in}$ does not have any effect on the output spectra. However, the electrons are more energetic at the end of the simulation for larger $\gamma'_{e,in}$: $\gamma'_e \sim 1.065$ for $\gamma'_{e,in} = 25$ and $\gamma'_e \sim 1.130$ for $\gamma'_{e,in} = 100$. Unlike previous simulations for $N_\gamma/N_e = 10^5$ [24], our output photon spectrum does not have a sharp drop in f_ν after $E_{\gamma,peak}$. The photon spectra show a power-law after the peak, $f_\nu \propto \nu^{-0.5}$ upto $\sim 10^3$ keV. After $\sim 10^4$ keV, f_ν for photons drops sharply by ~ 2 orders of magnitude. This is due to the fact that the average

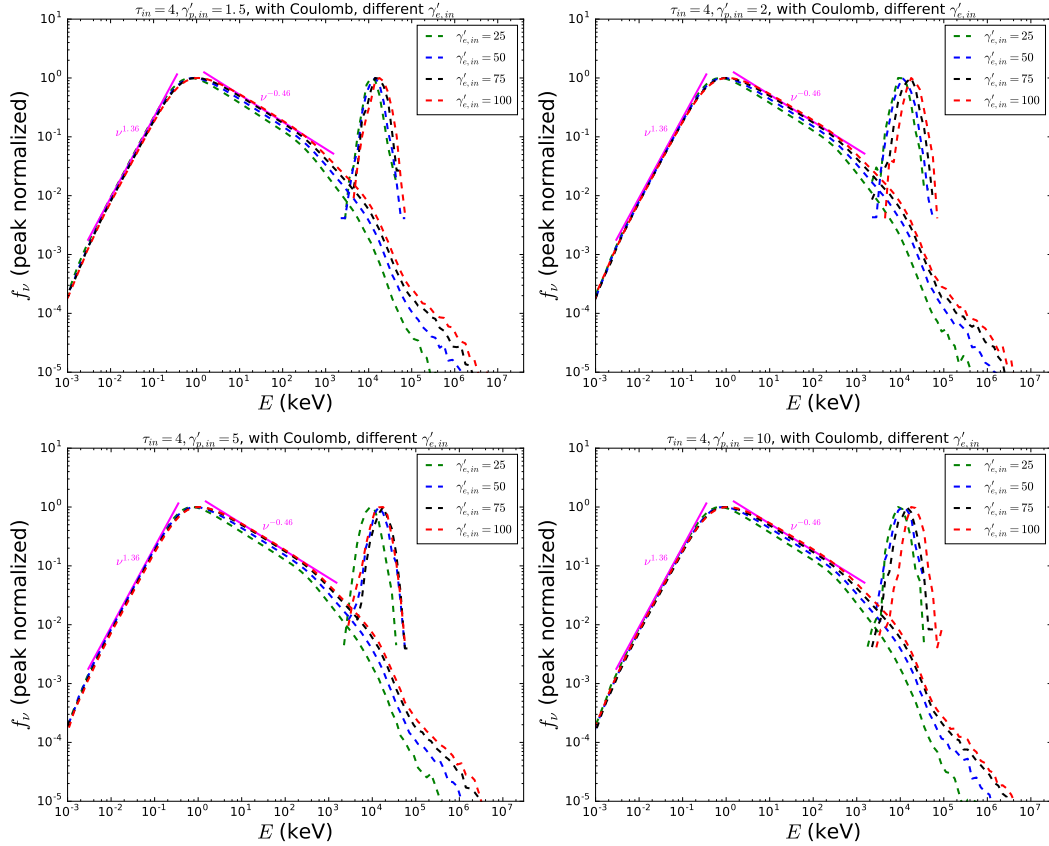


Figure 3.1: Simulation results for photons with seed spectrum given by Equation 2.1, $\tau_{in} = 4$ and with Coulomb interaction (both e-p and e-e). *Top-Left Panel:* For $\gamma'_{p,in} = 1.5$ and $\gamma'_{e,in} = 25, 50, 75$ and 100 . *Top-Right Panel:* For $\gamma'_{p,in} = 2$ and $\gamma'_{e,in} = 25, 50, 75$ and 100 . *Bottom-Left Panel:* For $\gamma'_{p,in} = 5$ and $\gamma'_{e,in} = 25, 50, 75$ and 100 . *Bottom-Right Panel:* For $\gamma'_{p,in} = 10$ and $\gamma'_{e,in} = 25, 50, 75$ and 100 .

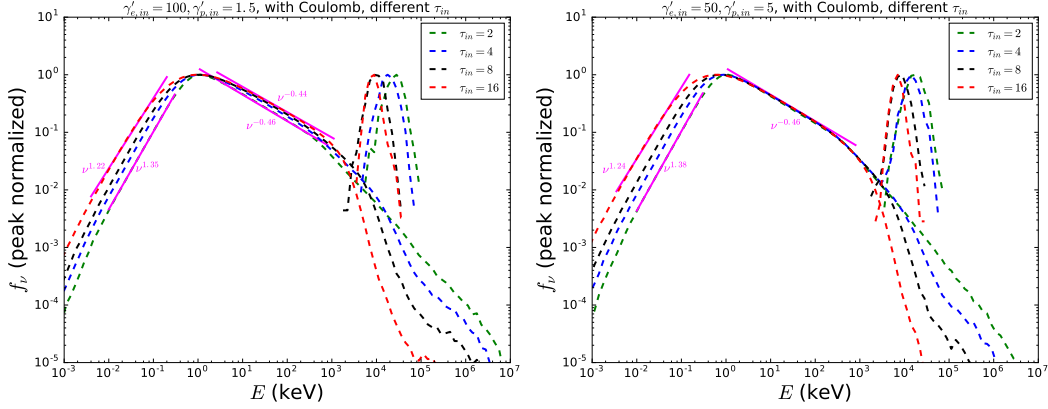


Figure 3.2: Comparison of simulation results for photons with seed spectrum given by Equation 2.1, with Coulomb interaction (e-p and e-e) and different $\tau_{in} = 2, 4, 8$ and 16 . *Left Panel:* For $\gamma'_{p,in} = 1.5$ and $\gamma'_{e,in} = 100$. *Right Panel:* For $\gamma'_{p,in} = 5$ and $\gamma'_{e,in} = 50$.

electron energy $\Gamma(\gamma'_{e,avg} - 1)m_e c^2$ is $\sim 10^4$ keV, beyond which enough photons cannot be upscattered by the electrons. The photon spectrum extends to higher energies for larger $\gamma'_{e,in}$ ($\sim 4 \times 10^5$ keV for $\gamma'_{e,in} = 25$ to $\sim 4 \times 10^6$ keV for $\gamma'_{e,in} = 100$) as the highest energy that a photon with energy $E'_{\gamma,peak}$ can get upscattered to after one scattering is $\sim E'_{\gamma,peak} \Gamma \gamma'^2_{e,in}$. More energetic electrons (with larger $\gamma'_{e,in}$) can transfer more energy to the photons which results in higher f_ν at large energies $\sim 10^4 - 10^7$ keV.

3.2 Effect of initial optical depth

In Figure 3.2, we present the simulation results for two different combinations of $\gamma'_{e,in}$ and $\gamma'_{p,in}$ for $\tau_{in} = 2, 4, 8$ and 16 when Coulomb (e-p and e-e) interaction is considered. As τ_{in} increases, the peak energy of the electron and

the photon output spectrum shifts to lower energies which is due to adiabatic cooling (see Equations 2.4 and 2.6). The energy of the electrons at the end of the simulation drops from $\gamma'_e \sim 1.196$ ($\gamma'_e \sim 1.130$) for $\tau_{in} = 2$ to $\gamma'_e \sim 1.052$ ($\gamma'_e \sim 1.046$) for $\tau_{in} = 16$ when $\gamma'_{p,in} = 1.5$ and $\gamma'_{e,in} = 100$ ($\gamma'_{p,in} = 5$ and $\gamma'_{e,in} = 50$). While there are smaller number of photons at higher energies for larger τ_{in} , the photon spectrum becomes slightly shallower at energies below $E_{\gamma,peak}$. As in the previous case considered, the photon spectrum shows a power-law $f_\nu \propto \nu^{-0.5}$ right after the peak and upto $\sim 10^3$ keV even though τ_{in} changes considerably. The output photon spectrum becomes shallower below $E_{\gamma,peak}$ for larger τ_{in} : $f_\nu \propto \nu^{1.4}$ for $\tau_{in} = 2$ to $f_\nu \propto \nu^{1.2}$ for $\tau_{in} = 16$. Multiple scatterings become more probable with increasing τ_{in} which results in photons getting scattered different number of times by the electrons before escaping out of the photosphere [40]. As a result, the output photon spectrum broadens and becomes shallower below $E_{\gamma,peak}$ (see Figure 3.6).

3.3 Effect of seed photon energy

In Figure 3.3, we present the simulation results for two different combinations of $\gamma'_{e,in}$ and $\gamma'_{p,in}$ for $\tau_{in} = 4$ when Coulomb (e-p and e-e) interaction is considered and $E'_{\gamma,peak} = h\nu'_{sa} = 0.2$ eV, 2 eV and 20 eV (see Equation 2.1). We find that the electron temperature at the end of the simulation is almost unaffected by the choice of $E'_{\gamma,peak}$ in the photon seed spectrum. This is because the electrons already cool down to non-relativistic γ'_e as there are enough scatterings with the photons for $\tau_{in} = 4$. The photon spectrum is

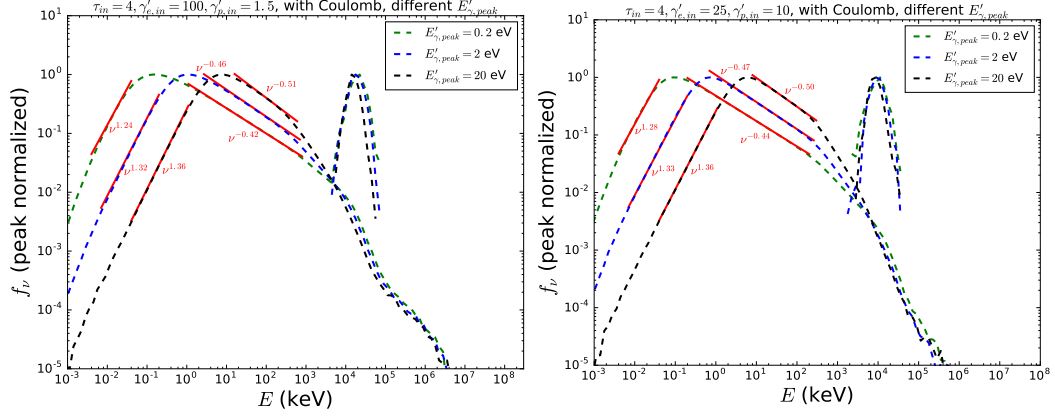


Figure 3.3: Comparison of simulation results for photons with seed spectrum given by Equation 2.1 and different $E'_{\gamma,peak} = h\nu'_{sa} = 0.2$ eV, 2 eV and 20 eV, for $\tau_{in} = 4$ and with Coulomb interaction (e-p and e-e). *Left Panel:* For $\gamma'_{p,in} = 1.5$ and $\gamma'_{e,in} = 100$. *Right Panel:* For $\gamma'_{p,in} = 10$ and $\gamma'_{e,in} = 25$.

broader for smaller $E'_{\gamma,peak}$ as most of the photons have smaller energy and can thus cool down the electrons more slowly. This results in more photons being upscattered to larger energies as the average number of scatterings per photon is higher. As a result, the photon spectrum is shallower above the peak for smaller $E'_{\gamma,peak}$: $f_{\nu} \propto \nu^{-0.5}$ for $E'_{\gamma,peak} = 20$ eV, $f_{\nu} \propto \nu^{-0.5}$ for $E'_{\gamma,peak} = 2$ eV and $f_{\nu} \propto \nu^{-0.4}$ for $E'_{\gamma,peak} = 0.2$ eV. At photon energies smaller than $E_{\gamma,peak}$, $f_{\nu} \propto \nu^{1.2} - \nu^{1.4}$ which becomes steeper for larger value of $E'_{\gamma,peak}$. The photons have a lower peak-energy at the end of the simulation as they cool down adiabatically.

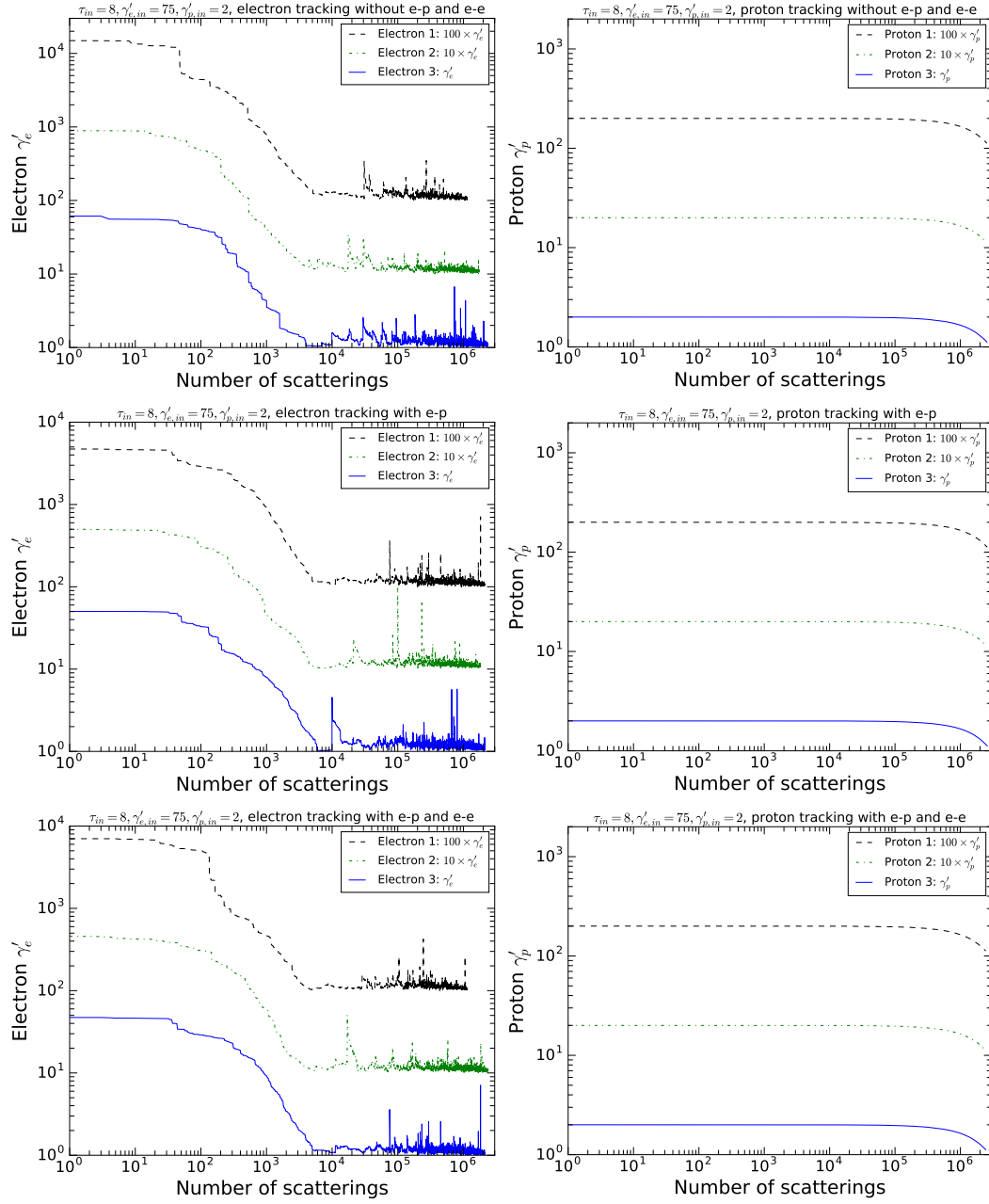


Figure 3.4: Evolution of γ'_e for 3 electrons and γ'_p for 3 protons, for photons with seed spectrum given by Equation 2.1 and $\tau_{in} = 8$, $\gamma'_{e,in} = 75$ and $\gamma'_{p,in} = 2$. *Top-Left and Top-Right Panels:* Without e-p and e-e interactions. *Middle-Left and Middle-Right Panels:* With e-p and without e-e interaction. *Bottom-Left and Bottom-Right Panels:* With e-p and e-e interactions.

3.4 Evolution of electron and proton energies

In Figure 3.4, we present the evolution of γ'_e (γ'_p) of 3 randomly selected electrons (protons) for $\tau_{in} = 8$, $\gamma'_{e,in} = 75$ and $\gamma'_{p,in} = 2$ when: 1) both e-p and e-e interactions are not considered, 2) only e-p interaction is considered and, 3) both e-p and e-e interactions are considered. The spikes in γ'_e correspond to the instances where the electron interacts either with a proton or a highly energetic photon resulting in a large transfer of energy to the electron. After each such instance, the energy of the electron falls back quickly to non-relativistic values when it upscatters a photon to transfer almost all the kinetic energy that was gained earlier. The electrons cool down very fast from $\gamma'_{e,in}$ to $\gamma'_e \sim 1$ as the IC timescale is much smaller than the dynamical timescale $t'_{dyn} = R/(\Gamma c)$ and the electron heating timescale $[(\gamma'_e - 1)m_e/(\gamma'_p - 1)m_p]t'_{p,Coul}$ for large γ'_e (see Equation 4.1). It can be seen that the 3 electrons experience different number of scatterings which is expected as electrons which are moving towards the photons are more likely to get scattered by the photons than the electrons which are moving away from the photons (Equation 2.12).

We compare γ'_e at the end of the simulation for the electron which experiences the largest number of scatterings for each of the three cases to find that e-p and e-e interactions do not have very significant effect on γ'_e : $\gamma'_e = 1.048$ without e-p and e-e, $\gamma'_e = 1.062$ with e-p and without e-e, $\gamma'_e = 1.059$ with e-p and e-e. The electrons get cooled down faster to small γ'_e ($\sim \gamma'_e$ without Coulomb) when e-e interaction is included in addition to e-p interaction as $t'_{e,Coul}$ is $\sim \beta_e/\beta_p$ times smaller than $[(\gamma'_e - 1)m_e/(\gamma'_p - 1)m_p]t'_{p,Coul}$. The

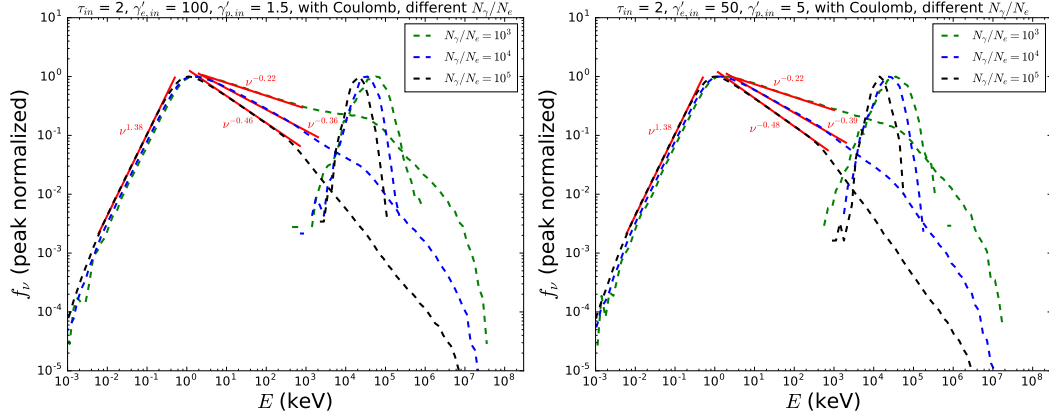


Figure 3.5: Comparison of simulation results for photons with seed spectrum given by Equation 2.1, $\tau_{in} = 2$ and with Coulomb interaction (e-p and e-e) for different $N_\gamma/N_e = 3 \times 10^6/3 \times 10^3$, $3 \times 10^7/3 \times 10^3$ and $3 \times 10^8/3 \times 10^3$. *Left Panel:* For $\gamma'_{p,in} = 1.5$ and $\gamma'_{e,in} = 100$. *Right Panel:* For $\gamma'_{p,in} = 5$ and $\gamma'_{e,in} = 50$.

protons have $\gamma'_p \sim 2$ for $\sim 10^6$ scatterings, beyond which their energy drops significantly due to adiabatic cooling. The protons cool down to $\gamma'_p = 1.123$ for all three cases (irrespective of whether Coulomb interaction is considered) as $t'_{ad} \sim t'_{dyn}$ is much smaller than $t'_{p,Coul}$ for large R towards the end of the simulation ($t'_{ad} \propto R$ whereas $t'_{p,Coul} \propto R^2$).

3.5 Effect of photon to electron number ratio

In Figure 3.5, we present the simulation results for two different combinations of $\gamma'_{e,in}$ and $\gamma'_{p,in}$ for $\tau_{in} = 2$ when Coulomb (e-p and e-e) interaction is considered and $N_\gamma/N_e = 3 \times 10^6/3 \times 10^3$, $3 \times 10^7/3 \times 10^3$ and $3 \times 10^8/3 \times 10^3$. We find that the electrons are considerably hotter at the end of the simulation for smaller N_γ/N_e : $\gamma'_e = 1.391$ (1.261) for $N_\gamma/N_e = 10^3$, $\gamma'_e = 1.196$ (1.144)

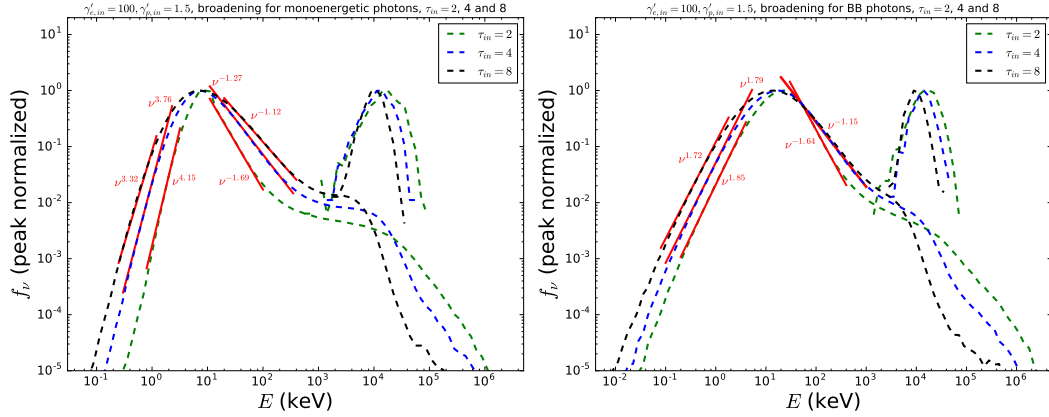


Figure 3.6: Broadening of seed photon spectrum for large $\tau_{in} = 2, 4$ and 8 , with Coulomb interaction (e-p and e-e), $\gamma'_{e,in} = 100$, $\gamma'_{p,in} = 1.5$, $N_\gamma = 10^8$ and $N_e = 10^3$. *Left Panel:* For monoenergetic photon seed spectrum with $E'_{\gamma,peak} = 20$ eV. *Right Panel:* For blackbody (BB) photon seed spectrum with $E'_{\gamma,peak} = 20$ eV.

for $N_\gamma/N_e = 10^4$ and $\gamma'_e = 1.130$ (1.091) for $N_\gamma/N_e = 10^5$ when $\gamma'_{e,in} = 100$ and $\gamma'_{p,in} = 1.5$ ($\gamma'_{e,in} = 50$ and $\gamma'_{p,in} = 5$). This is expected as the electrons cool down faster when there are more photons available to get upscattered. As a result, the photon spectrum becomes shallower above $E_{\gamma,peak}$ as more photons get upscattered by the slowly cooling electrons to higher energies for smaller N_γ/N_e : $f_\nu \propto \nu^{-0.5}$ for $N_\gamma/N_e = 10^5$, $f_\nu \propto \nu^{-0.4}$ for $N_\gamma/N_e = 10^4$ and $f_\nu \propto \nu^{-0.2}$ for $N_\gamma/N_e = 10^3$ from the peak energy upto $\sim 10^3$ keV.

3.6 Effect of geometrical broadening

In Figure 3.6, we present the simulation results for the broadening of mono-energetic and blackbody seed photon spectra with $E'_{\gamma,peak} = 20$ eV, $\gamma'_{e,in} = 100$ and $\gamma'_{p,in} = 1.5$ when $\tau_{in} = 2, 4$ and 8 . As expected, the electrons

have smaller energy at the end of the simulation for larger τ_{in} : $\gamma'_{e,in} = 1.130$ ($\gamma'_{e,in} = 1.117$) for $\tau_{in} = 2$, $\gamma'_{e,in} = 1.065$ ($\gamma'_{e,in} = 1.091$) for $\tau_{in} = 4$ and $\gamma'_{e,in} = 1.052$ ($\gamma'_{e,in} = 1.052$) for $\tau_{in} = 8$ for mono-energetic (blackbody) seed photons. The photon spectrum becomes considerably broader with increasing τ_{in} : $f_\nu \propto \nu^{4.2}$ ($f_\nu \propto \nu^{1.9}$) for $\tau_{in} = 2$ to $f_\nu \propto \nu^{3.3}$ ($f_\nu \propto \nu^{1.7}$) for $\tau_{in} = 8$ below $E_{\gamma,peak}$ and $f_\nu \propto \nu^{-1.7}$ ($f_\nu \propto \nu^{-1.6}$) for $\tau_{in} = 2$ to $f_\nu \propto \nu^{-1.1}$ ($f_\nu \propto \nu^{-1.2}$) for $\tau_{in} = 8$ above $E_{\gamma,peak}$ for mono-energetic (blackbody) seed photons. Unlike previous simulations, the power-law above $E_{\gamma,peak}$ only extends up to $E_\gamma \sim 10^2$ keV.

To summarize, we studied the effect of $\gamma'_{e,in}$, $\gamma'_{p,in}$, τ_{in} , $E'_{\gamma,peak}$, N_γ/N_e and Coulomb (e-p and e-e) interaction on the output spectrum of the photons and the electrons. In Figure 3.1, we show that $\gamma'_{e,in}$ and $\gamma'_{p,in}$ do not have any significant effect on $E'_{\gamma,peak}$ and the power-law above peak energy except that the high-energy tails in the photon spectrum extend to larger energies for larger $\gamma'_{e,in}$. In Figure 3.2, we find that increasing τ_{in} slightly flattens the photon spectrum at low energies although f_ν drops faster at higher energies. In Figure 3.3, we find that the peak energy of the seed photon spectrum determines the peak energy and shape of the output photon spectrum. In Figure 3.4, we track γ'_e to establish that e-p and e-e interactions do not affect the electron energies significantly which is in good agreement with the previous simulations (Figures 3.1 - 3.3). In Figure 3.5, we find that although $E'_{\gamma,peak}$ is unaffected by the decrease in N_γ/N_e , f_ν increases significantly above $E'_{\gamma,peak}$ resulting in shallower photon spectrum. In Figure 3.6, we find that the output

photon spectrum is broadened for large τ_{in} irrespective of the choice of the seed photon spectrum. This implies that the output photon spectrum for high $\tau_{in} \sim$ few tens - hundred will be in good agreement with the observed Band spectrum.

Chapter 4

Discussion of results

In this chapter, we first discuss the simulation parameters that significantly affect the output photon spectrum. Then we discuss the energy constraint that the electrons must satisfy in order to transfer enough energy to the photons so that a power-law can be produced above $E_{\gamma,peak}$. Although this constraint is a necessary condition, it is not a sufficient condition to ensure a power-law spectrum for photons at high energies [24]. Next, we discuss the evolution of energies for the photons, protons and the electrons due to processes such as Comptonization, adiabatic cooling and Coulomb interaction (e-p and e-e) during the expansion of the relativistic jet. We also evaluate the equilibrium γ'_e when the electrons are cooled due to IC and are heated by the protons due to e-p interaction. Lastly, we discuss the effect of N_γ/N_e on our simulation results.

4.1 Effect of simulation parameters on the output spectrum

In our simulations, the parameters that mainly affect the output photon spectrum are $\gamma'_{e,in}$, $\gamma'_{p,in}$, $E'_{\gamma,peak} = h\nu'_{sa}$, τ_{in} and N_γ/N_e . The e-p interaction slightly elevates the energy of the electrons but it does not change the photon

spectrum and the proton energies appreciably. The e-e interaction plays an important role in redistributing energy among the electrons after they are heated by the e-p interactions.

$\gamma'_{e,in}$ and $\gamma'_{p,in}$ determine the amount of energy that the electrons can transfer to the photons through Comptonization and the amount of energy that the protons can transfer to the electrons through e-p interactions, respectively. Higher $\gamma'_{p,in}$ can also result in more energetic photons as the electrons will gain more energy from the protons to transfer it to the photons. However, for most part of the simulations, $[(\gamma'_e - 1)m_e/(\gamma'_p - 1)m_p]t'_{p,Coul}$ is of the same order as IC timescale in the jet-comoving frame which is given by,

$$t'_{IC} = \frac{3(\gamma'_e - 1)m_e c}{4 U'_\gamma \sigma_T \gamma_e'^2 \beta_e'^2} \quad (4.1)$$

where $U'_\gamma = L_\gamma/(4\pi R^2 \Gamma^2 c)$ is the radiation energy density. Hence, the electrons attain an equilibrium γ'_e after a certain number of scatterings and Coulomb interaction is relatively unimportant in determining the shape of the output photon spectrum.

$E'_{\gamma,peak}$ is also an important parameter that affects the shape of the output photon spectrum. However for almost all our simulations (except Figure 3.3), we fix the seed photon spectrum (as given by Equation 2.1) to study the effect of other parameters and interactions better. As a photon can be upscattered to an energy $\sim E'_{\gamma,peak} \Gamma \gamma_e'^2$ after one scattering, more energetic photons (with higher $E'_{\gamma,peak}$) cool the electrons faster after multiple scatterings. We do not consider electron-positron pair production for our simulations

as $E'_{\gamma,peak} \sim 0.2 - 20$ eV is much less than the rest mass energy of the electrons in the jet-comoving frame (see Appendix C, for more details).

The average number of scatterings experienced by a photon before escaping the photosphere is $\sim 2\tau_{in}$ [35] and hence τ_{in} also determines the shape of the output photon spectrum. For larger τ_{in} , the electrons and the protons cool down more adiabatically (see Equations 2.4 and 2.5). The photons get scattered multiple times thus increasing the probability of different photons getting scattered different number of times before escaping the photosphere. This results in broadening of the photon spectrum and the output photon spectrum looks shallower below $E_{\gamma,peak}$. This broadening of the output photon spectrum at large τ_{in} is independent of the choice of the seed photon spectrum (see Figure 3.6).

Another parameter which affects the photon and electron energies is N_{γ}/N_e . For smaller N_{γ}/N_e , there are more electrons to upscatter the photons to higher energies. Moreover, $N_e = N_p$ implies that there are more protons to transfer energy to the electrons. Hence, the output photon spectrum has more photons at higher energies resulting in a shallower spectrum above $E_{\gamma,peak}$.

It should be noted that unlike previous simulations [22, 24], we do not re-accelerate the electrons back to their initial distribution after every few scattering events. Rather the electrons are redistributed to MB distribution whose peak temperature is determined using $\gamma'_{e,avg}$ after each scattering event. We do not consider any external dissipation events for electron heating except the energy transfer from the protons to the electrons.

4.2 Energy constraint for power-law above $E'_{\gamma,peak}$

Now we discuss the constraint that $\gamma'_{e,in}$ and $\gamma'_{p,in}$ need to satisfy in order to have a power-law spectrum above $E'_{\gamma,peak}$. The total initial kinetic energy of the electrons and the protons at the beginning of the simulation is $(\gamma'_{e,in} - 1)N_e m_e c^2$ and $(\gamma'_{p,in} - 1)N_p m_p c^2$, respectively. The energy available to the electrons should at least be as large as the energy gain that is required by the photons to populate the high-energy tail. The energy transferred from the protons to the electrons in the course of the jet expansion is $\sim (t'_{dyn}/t'_{p,Coul})(\gamma'_{p,in} - 1)N_p m_p c^2$. In order to have a power-law spectrum above $E'_{\gamma,peak}$, the energy of a fraction $\sim f$ of the photons near peak-energy $E'_{\gamma,peak}$ has to increase by a factor $\sim f$. Assuming that most of the photons have energies close to the photon peak-energy $E'_{\gamma,peak}$, the electron $\gamma'_{e,in}$ and the proton $\gamma'_{p,in}$ should satisfy the energy constraint given by

$$(\gamma'_{e,in} - 1)N_e m_e c^2 + \frac{t'_{dyn}}{t'_{p,Coul}}(\gamma'_{p,in} - 1)N_p m_p c^2 \gtrsim f \frac{N_\gamma}{f} E'_{\gamma,peak} \quad (4.2)$$

For our simulations, $E'_{\gamma,peak} = 2$ eV, $N_\gamma = 10^8$ and $N_p = N_e = 10^3$. t'_{dyn} and $t'_{p,Coul}$ are evaluated when most of the scatterings occur with $\gamma'_e \sim 1$ and $\gamma'_p \sim \gamma'_{p,in}$ (see Figure 3.4). For this choice of parameters, the above condition is satisfied for $\gamma'_{e,in} \sim 25 - 100$ and $\gamma'_{p,in} \sim 1.5 - 10$ that we have considered. This explains the power-law spectrum from $E'_{\gamma,peak}$ upto $\sim 10^3$ keV in all our simulations.

4.3 Energy evolution for the photons, protons and electrons

Now we discuss the evolution of energy for the photons, protons and electrons to explain our simulation results.

4.3.1 Photons

The photons gain energy from the electrons through Comptonization and cool due to adiabatic expansion. The IC timescale is much smaller compared to $t'_{ad} \sim t'_{dyn}$ until the electrons cool down to non-relativistic energies ($\gamma'_e \sim 1$). Although some photons are upscattered to high energies through Comptonization when the electrons are hot, the peak of the photon spectrum is affected only by adiabatic cooling and not IC cooling. This is expected as most of the scatterings occur after the electrons already cool down to non-relativistic energies making Comptonization unimportant for determining $E'_{\gamma,peak}$ in the output photon spectrum.

The peak-energy of the output photon spectrum can be obtained using Equations 2.3 and 2.6,

$$\frac{E'_{\gamma,peak,f}}{E'_{\gamma,peak,i}} = \left(\frac{R_{ph}}{R_{in}} \right)^{-2/3} = \tau_{in}^{-2/3} \quad (4.3)$$

where $E'_{\gamma,peak,i}$ ($E'_{\gamma,peak,f}$) is the peak-energy of the initial (final) photon spectrum in the jet-comoving frame. This is in good agreement with our simulation results for different τ_{in} and $E'_{\gamma,peak}$ in Figures 3.2 and 3.3.

4.3.2 Protons

The protons lose energy to the electrons through e-p interaction in addition to cooling adiabatically as the jet expands. The proton cooling timescale $t'_{p,Coul}$ is much larger compared to t'_{ad} when the electrons are relativistic (see Equation 2.7). After the electrons cool down to non-relativistic energies, $t'_{p,Coul} \propto (\gamma'_p - 1)(\beta'_p/n'_e) \propto R^2$ which increases faster compared to $t'_{ad} \propto R$ with the expansion of the jet. Thus, e-p interaction is relatively unimportant in determining the final energy of the protons which is actually determined by adiabatic cooling. From Figure 3.4, we can see that $\gamma'_p \sim 2$ for most part of the simulation. Thus, we can write using Equation 2.5,

$$\frac{\gamma'_{p,f} - 1}{\gamma'_{p,i} - 1} \sim \left(\frac{R_{ph}}{R_{in}} \right)^{-1} = \tau_{in}^{-1} \quad (4.4)$$

as $\gamma'_{ad,p} \sim 3/2$. For $\tau_{in} = 8$ and $\gamma'_{p,in} = 2$ as used in the simulations in Figure 3.4, $\gamma'_{p,f} = 1.125$ which is in very good agreement with the γ'_p value that we find by tracking the protons in Figure 3.4.

4.3.3 Electrons

While the electrons gain energy from the protons through e-p interaction, they also lose energy due to adiabatic expansion of the jet and Comptonization. Comptonization of electrons no longer decreases the energy of the electrons significantly after γ'_e drops to $\gamma'_{e,Comp} = 1 + 1/(8\tau_{in})$ [24]. Here we estimate the change in energy of the electrons due to the three processes: adiabatic cooling, Comptonization and e-p interaction, after the electrons have cooled down to $\gamma'_{e,Comp}$ to explain our simulation results in Figure 3.4.

The evolution of γ'_e due to adiabatic cooling is given by Equation 2.4. After the electrons have already cooled down to $\gamma'_e \sim 1$ the energy change due to adiabatic cooling is,

$$\frac{\gamma'_{e,f} - 1}{\gamma'_{e,i} - 1} \sim \left(\frac{R_{ph}}{R_{in}} \right)^{-4/3} = \tau_{in}^{-4/3} \quad (4.5)$$

as $\gamma'_{ad,e} \sim 5/3$. For $\tau_{in} = 8$ and $\gamma'_{e,i} = \gamma'_{e,Comp} \sim 1.016$ as used in simulations in Figure 3.4, $\gamma'_{e,f} \sim 1.001$. To estimate the change in γ'_e due to Comptonization and Coulomb heating by the protons, we first evaluate the corresponding timescales along with the dynamical timescale (all timescales averaged over R) for $\tau_{in} = 8$. For $\gamma'_e = \gamma'_{e,Comp}$ and $\gamma'_p \sim 2$, the R -averaged timescales are,

$$\langle t'_{dyn} \rangle_R = \left\langle \frac{R}{\Gamma_C} \right\rangle_R = 0.05 \text{ s} \quad (4.6)$$

$$\langle t'_{IC} \rangle_R = \left\langle \frac{3}{8} \frac{m_e c}{U'_\gamma \sigma_T \gamma'_{e,Comp}} \right\rangle_R = 1.25 \times 10^{-4} \text{ s} \quad (4.7)$$

$$\langle t'_{Coul} \rangle_R = \left\langle \frac{(\gamma'_{e,Comp} - 1) m_e c^2}{5 \times 10^{-19} n'_e} \beta'_p \right\rangle_R = 2.82 \times 10^{-5} \text{ s} \quad (4.8)$$

The final energy of the electrons after $t = \langle t'_{dyn} \rangle_R$ due to IC is given by,

$$E'_{e,f,IC} = E'_{e,i} e^{-\langle t'_{dyn} \rangle_R / \langle t'_{IC} \rangle_R} \quad (4.9)$$

which reduces to,

$$\gamma'_{e,f,IC} = 1 + (\gamma'_{e,Comp} - 1) e^{-400} \sim 1 \quad (4.10)$$

γ'_e of the electrons after $t = \langle t'_{dyn} \rangle_R$ due to Coulomb heating by the protons is,

$$\gamma'_{e,f,Coul} = 1 + (\gamma'_{e,Comp} - 1) e^{\langle t'_{dyn} \rangle_R / \langle t'_{Coul} \rangle_R} \gg \gamma'_{e,Comp} \quad (4.11)$$

Thus, we find that the electron heating due to the Coulomb interaction is faster than the rate of Comptonization of the electrons at smaller values of $\tau \sim 1$ i.e. towards the end of the simulation. This explains our results in Figure 3.4 as γ'_e obtained at the end of the simulation is higher when e-p interaction is considered.

4.4 Equilibrium γ'_e of electrons

In this section, we evaluate γ'_e after the electrons reach equilibrium due to Coulomb heating and Comptonization. As the timescale for adiabatic cooling of electrons $\sim t'_{dyn}$ is much longer as compared to t'_{IC} and t'_{Coul} , we can neglect adiabatic cooling while considering the equilibrium of the electrons. Equating the IC energy loss rate with the Coulomb energy gain rate for the electrons gives,

$$\frac{5 \times 10^{-19} n'_e \beta_p'^2}{8.3 \times 10^{-15} [(\gamma'_e - 1) m_e c^2 / k_B]^{3/2} + \beta_p'^3} = \frac{4}{3} U'_\gamma \sigma_T (\gamma_e'^2 - 1) c \quad (4.12)$$

Using the expressions for n'_e , U'_γ and $\gamma'_p = 1.123$, we obtain

$$39.07(\gamma'_e - 1)^{3/2} + 1 = \frac{0.273}{\gamma_e'^2 - 1} \quad (4.13)$$

which gives $\gamma'_e = 1.074$. Thus, the equilibrium γ'_e is close to $\gamma'_e = 1.062$ obtained in Figure 3.4 when e-p interaction is considered. The equilibrium γ'_e is slightly higher than γ'_e obtained at the end of the simulations for Figure 3.4 which is expected as we neglect adiabatic cooling and e-e interaction for our equilibrium calculations.

In our analysis, we have assumed that the electrons always cool due to IC and neglect the possibility that an energetic photon can transfer energy back to the electrons. However, there are about ~ 10 instances in each of the three cases (without e-p and e-e, with e-p and with e-p and e-e) when the electron energy increases to $\gamma'_e \sim 2$. As a result, more photons are upscattered to higher energies and the power-law $f_\nu \propto \nu^{-0.5}$ extends to $\sim 10^3$ keV for almost all our simulations. In addition, the Compton-Y parameter for sub-relativistic electrons [41] is,

$$Y = 2\tau_{in} \times \frac{4k_B T'_e}{m_e c^2} \sim 8\tau_{in} \times (\gamma'_e - 1) \quad (4.14)$$

which is ~ 4 at the end of the simulation for $\gamma'_e \sim 1.062$ and $\tau_{in} = 8$ (see Figure 3.4) - large enough to upscatter most of the photons by a factor of 2 in energy and populate the high-energy tail of the photon spectrum. The considerably large value of Compton-Y parameter accounts for the upscattering of photons near $E_{\gamma,peak}$ to the high energy power-law region of the photon spectrum.

4.5 Effect of N_γ/N_e on simulation results

In this section, we discuss the simulation results in Figure 3.5 which were performed at $\tau_{in} = 2$ and different values of $N_\gamma/N_e = 10^3, 10^4$ and 10^5 for two different combinations of $\gamma'_{e,in}$ and $\gamma'_{p,in}$. The number of electrons $N_e = 3 \times 10^3$ is kept constant for the simulations and $N_\gamma (= 3 \times 10^6, 3 \times 10^7$ and $3 \times 10^8)$ is varied. We find that the electrons are hotter and the photon spectrum is shallower for smaller N_γ/N_e for both combinations of $\gamma'_{e,in}$ and $\gamma'_{p,in}$ considered

in Figure 3.5. Rewriting Equation 4.2 using Equation 2.7 and the fact that $N_p = N_e$,

$$(\gamma'_{e,in} - 1)m_e c^2 + \frac{5 \times 10^{-19} n'_e R}{\beta'_{p,in}} \frac{R}{\Gamma c} \gtrsim \frac{N_\gamma}{N_e} E'_{\gamma,peak} \quad (4.15)$$

Thus, for a given $\gamma'_{e,in}$, $\gamma'_{p,in}$ and $E'_{\gamma,peak}$, the electrons cannot transfer enough energy to the photons to populate the higher energy power-law tail for larger N_γ/N_e . As a result, the photon spectrum falls down faster at higher energies for larger values of N_γ/N_e . Our simulations show that the photon spectrum is significantly affected by the choice of N_γ/N_e and it is important to perform the simulations with realistic values of $N_\gamma/N_e = 10^5$. For all three values of N_γ/N_e we have more photons just above the peak photon energy as compared to previous simulations [22, 24], which is due to smaller $E'_{\gamma,peak}$ resulting in slower cooling of the electrons by the photons.

Chapter 5

Conclusions

We studied photospheric emission for GRB prompt emission using a MC code with photon to electron number ratio $N_\gamma/N_e = 10^5$, which is close to the expected value for a typical GRB if the radiation efficiency is $\sim 10\%$. Our objective was to find out whether photospheric emission can explain the observed non-thermal low ($f_\nu \propto \nu^0$) and high-energy ($f_\nu \propto \nu^{-1.2}$) spectrum of GRB prompt emission. For all our simulations, we considered Comptonization of seed photons with synchrotron spectrum in fast cooling regime. The electrons are continuously heated by the mono-energetic protons as the electrons interact with the protons (e-p) and other electrons (e-e) through Coulomb interaction. In all our simulations, we also consider the energy change for electrons, photons and protons due to the adiabatic expansion of the jet. We find that the output photon spectrum exhibits a power-law extending upto $\sim 10^3$ keV from $E'_{\gamma,peak}$ for the parametric space of initial electron energy ($\gamma'_{e,in}$), initial proton energy ($\gamma'_{p,in}$) and initial optical depth (τ_{in}) that we consider in this work.

We find that the output photon spectrum becomes slightly shallower below $E'_{\gamma,peak}$ as the initial optical depth τ_{in} increases. This is expected as

photons get scattered by electrons different number of times before escaping out of the photosphere as τ_{in} increases. This can possibly result in an output photon spectrum which is in good agreement with the observed low-energy spectrum $f_\nu \propto \nu^0$ of the prompt emission, especially at large $\tau_{in} \sim$ few tens-hundred. The flattening of the output photon spectrum below $E'_{\gamma,peak}$ for large τ_{in} is independent of the choice of seed photon spectrum. We find that the peak energy and shape of the output photon spectrum is also determined by the peak energy $E'_{\gamma,peak}$ of the seed photon spectrum. The peak energy in the output spectrum reduces by a factor $\sim \tau_{in}^{-2/3}$ compared to the seed spectrum because of adiabatic cooling of photons. As expected, the photon spectrum is broader around the peak energy for smaller $E'_{\gamma,peak}$ because the photons are less energetic in the jet-comoving frame and can cool the electrons more slowly resulting in more scatterings.

We track the electrons and the protons to study the effect of Coulomb (e-p and e-e) interaction on the electron and proton energies and the output photon spectrum. We find that the electron energies are slightly elevated in the presence of Coulomb interaction and the protons cool down considerably by the end of the simulation due to adiabatic expansion of the jet for the optical depths that we consider. The presence of Coulomb interaction does not affect $E'_{\gamma,peak}$ and the shape of the output photon spectrum (both below and above $E_{\gamma,peak}$) in general. We evaluate γ'_e at equilibrium due to IC and e-p interactions and find that Compton-Y parameter ~ 4 at the end of the simulation - which is large enough to populate the high-energy power-law tail

of the photon spectrum.

We also performed simulations for different N_γ/N_e and found that the photon spectrum becomes shallower above $E'_{\gamma,peak}$ and does not exhibit power-law tail at high energies for smaller N_γ/N_e . This shows the importance of performing simulations with realistic N_γ/N_e and thus radiation efficiency η . We find that the Comptonization of seed photons with synchrotron spectrum in fast cooling regime cannot explain the high energy power-law dependence ($f_\nu \propto \nu^{-1.2}$) and the peak energy of the observed GRB prompt emission spectrum. However, $f_\nu \propto \nu^0$ for the photon spectrum below $E_{\gamma,peak}$ can be successfully explained using fast cooling synchrotron seed photon spectrum at very large optical depths ($\tau_{in} \sim 100$).

Appendices

Appendix A

Initialization of photon energy

Here we describe the algorithm that we implemented to draw seed photons from synchrotron spectrum for fast cooling electrons. The energy distribution is given by Equation 2.1 with break energies $E'_{\gamma,1} = h\nu_l$, $E'_{\gamma,2} = h\nu_{ac}$, $E'_{\gamma,3} = h\nu_{sa}$, $E'_{\gamma,4} = h\nu_m$ and $E'_{\gamma,5} = h\nu_u$. We denote the spectral indices between the break energies using $p_1 = -1.0$, $p_2 = 2.0/3.0$, $p_3 = 1.5$ and $p_4 = 4.5/2.0$ where the photon spectrum is given by $f_\nu \propto \nu^{1-p}$.

We first evaluate,

$$\begin{aligned}
 C_1 &= \frac{E_1^{1-p_1} - E_2^{1-p_1}}{p_1 - 1} \\
 C_2 &= \left(\frac{E_2^{1-p_2} - E_3^{1-p_2}}{p_2 - 1} \right) E_2^{p_2-p_1} \\
 C_3 &= \left(\frac{E_3^{1-p_3} - E_4^{1-p_3}}{p_3 - 1} \right) E_2^{p_2-p_1} E_3^{p_3-p_2} \\
 C_4 &= \left(\frac{E_4^{1-p_4} - E_5^{1-p_4}}{p_4 - 1} \right) E_2^{p_2-p_1} E_3^{p_3-p_2} E_4^{p_4-p_3}
 \end{aligned}$$

to find $K_1 = C_1/(C_1 + C_2 + C_3 + C_4)$, $K_2 = (C_1 + C_2)/(C_1 + C_2 + C_3 + C_4)$ and $K_3 = (C_1 + C_2 + C_3)/(C_1 + C_2 + C_3 + C_4)$. Next, we draw two random

numbers ξ_1 and ξ_2 between 0 and 1 to set

$$E'_\gamma = \begin{cases} [\xi_2(E'_{\gamma,2}{}^{1-p_1} - E'_{\gamma,1}{}^{1-p_1}) + E'_{\gamma,1}{}^{1-p_1}]^{1/(1-p_1)}, & 0 < \xi_1 < K_1 \\ [\xi_2(E'_{\gamma,3}{}^{1-p_2} - E'_{\gamma,2}{}^{1-p_2}) + E'_{\gamma,2}{}^{1-p_2}]^{1/(1-p_2)}, & K_1 < \xi_1 < K_2 \\ [\xi_2(E'_{\gamma,4}{}^{1-p_3} - E'_{\gamma,3}{}^{1-p_3}) + E'_{\gamma,3}{}^{1-p_3}]^{1/(1-p_3)}, & K_2 < \xi_1 < K_3 \\ [\xi_2(E'_{\gamma,5}{}^{1-p_4} - E'_{\gamma,4}{}^{1-p_4}) + E'_{\gamma,4}{}^{1-p_4}]^{1/(1-p_4)}, & K_3 < \xi_1 < 1 \end{cases}$$

Appendix B

Electron-photon scattering probability

In this Appendix, we describe the algorithm to select an electron for scattering with a photon using the scattering probability P_{scatt} . We denote the angle between the propagation directions of a particular electron among N_e electrons and the photon (already selected from the priority queue, see Section 2.5) in the jet-comoving frame before scattering by θ'_e . The differential number of scatterings experienced by the photon in time dt' in jet-comoving frame is then given by,

$$dN'_{scatt} = dn'_e \sigma_{TC} (1 - \beta'_e \cos \theta'_e) dt'$$

where, $dn'_e = f(\beta'_e, \Omega'_e) d^3 \beta'_e d\Omega'_e$ is differential element corresponding to the electron number density in the jet-comoving frame. $f(\beta'_e, \Omega'_e)$ corresponds to the energy distribution of the electrons which is MB and $d^3 \beta'_e d\Omega'_e = \beta_e'^2 d\beta'_e \sin \theta'_e d\theta'_e d\phi'_e$ is the differential element in the velocity space of the electrons. The probability of scattering between an electron and the photon is,

$$P_{scatt}(\beta'_e, \theta'_e) \propto \frac{d\nu'_{scatt}}{\beta_e'^2 d\beta'_e d\Omega'_e} = f(\beta'_e, \theta'_e) \sigma_{TC} (1 - \beta'_e \cos \theta'_e)$$

where $d\nu'_{scatt}$ is the differential frequency of electron-photon scattering. P_{scatt} is independent of ϕ'_e because of azimuthal symmetry of the scattering event in the

jet-comoving frame. Assuming that the electron distribution stays isotropic between scattering events

$$P_{scatt}(\beta'_e, \theta'_e) \propto e^{-c\beta_e'^2} (1 - \beta'_e \cos \theta'_e)$$

where, c is a constant determined by the temperature of the electrons. The normalized probability can then be written as,

$$P_{scatt}(\beta'_e, \theta'_e) = \frac{1}{4\pi\beta_e'^2} (1 - \beta'_e \cos \theta'_e)$$

The cumulative distribution function corresponding to the above probability distribution is,

$$F_{scatt}(\beta'_e, \theta'_e) = \frac{1}{2}\beta'_e \left[(1 - \cos\theta'_e) + \frac{1}{4}\beta'_e (\cos^2\theta'_e - 1) \right]$$

which is zero for $\theta'_e = 0$ and β'_e for $\theta'_e = \pi$. Next, we draw a random number ξ_3 between 0 and $N_e - 1$ and evaluate $|\xi_3 - N_e F_{scatt}(\theta'_e)|$ for all N_e electrons. The electron selected for scattering with the photon is the one with minimum value of $|\xi_3 - N_e F_{scatt}(\theta'_e)|$.

Appendix C

Pair production and annihilation

The fraction of photons with sufficient energy, $E_\gamma \sim m_e c^2 \Gamma \sim 1.5 \times 10^5$ keV, needed to create pairs in the jet is $f_\nu \sim 10^{-4}$ for $\tau_{in} = 4$ (see Fig. 3.1). Let η be the fraction of photons that are close to the peak photon energy, $E_{\gamma,peak} = \Gamma h \nu'_{sa}$, and within an energy range: $E_{\gamma,1} = \Gamma h(0.75\nu'_{sa})$ to $E_{\gamma,2} = \Gamma h(1.25\nu'_{sa})$. Then the number of photons with sufficient energy to produce pairs is, $N_{\gamma,MeV} \sim 10^{-4} \eta N_{\gamma,tot}$, where $N_{\gamma,tot} = 10^8$ is the total number of photons in the jet.

The optical depth for pair production is, $\tau_{\gamma\gamma,MeV} \sim (N_{\gamma,MeV} \sigma_{\gamma\gamma,avg}) / (4\pi R^2)$, where $\sigma_{\gamma\gamma,avg} = \int_{y_{min}}^{y_{max}} \sigma_{\gamma\gamma}(y) (f_y/y) dy / \int_{y_{min}}^{y_{max}} (f_y/y) dy$ is the average pair production cross section with $y^2 = \frac{1}{2} \frac{h\nu'_1}{m_e c^2} \frac{h\nu'_2}{m_e c^2} (1 - \cos \theta)$. Here, ν'_i denotes the energy of the incoming photons and θ is the angle between them. Assuming isotropic photon distribution i.e. $\langle \cos \theta = 0 \rangle$, we have $y_{min} = 1$, $y_{max} \sim 0.7(E_{\gamma,max}/\Gamma m_e c^2) \sim 50$ and $f_y \propto y^{-1.25}$ as the maximum possible photon energy $E_{\gamma,max} \sim 10^7$ keV from our simulation results. The average pair production cross section is then [40]

$$\sigma_{\gamma\gamma,avg} = \frac{\int_1^{50} \sigma_{\gamma\gamma} y^{-2.25} dy}{\int_1^{50} y^{-2.25} dy} \sim 0.16 \sigma_T \quad (C.1)$$

where

$$\sigma_{\gamma\gamma} = \frac{3}{8} \frac{\sigma_T}{y^2} \left[\left(2 + \frac{2}{y^2} - \frac{1}{y^4} \right) \ln(y + \sqrt{y^2 - 1}) - \left(1 + \frac{1}{y^2} \right) \left(1 - \frac{1}{y^2} \right)^{1/2} \right]$$

Substituting $N_{\gamma, MeV}$ and $\sigma_{\gamma\gamma, avg}$,

$$\tau_{\gamma\gamma, MeV} \sim 10^{-4} \eta \left(\frac{N_{\gamma, tot}}{N_{e, tot}} \right) \left(\frac{\sigma_{\gamma\gamma, avg} N_{e, tot}}{4\pi R^2} \right) \sim 10\eta \times 0.16\tau_e \sim 1.6\eta\tau_e \quad (\text{C.2})$$

where we used $N_{\gamma, tot}/N_{e, tot} = 10^5$ and $\tau_e \sim (N_{e, tot}\sigma_T)/(4\pi R^2)$. Therefore, $\tau_{\gamma\gamma, MeV} \lesssim 1$ is satisfied as long as $\eta \lesssim 1/6$ (for $\tau_{in} \sim 4$).

For the synchrotron seed spectrum of fast cooled electrons that we consider

$$\eta \sim \frac{\int_{0.75\nu'_{sa}}^{1.25\nu'_{sa}} (f_\nu/\nu) d\nu}{\int_{\nu'_{ac}}^{\nu'_m} (f_\nu/\nu) d\nu} \sim \frac{\int_{0.75\nu'_{sa}}^{\nu'_{sa}} (\nu/\nu_{sa})^{3/8} d\nu + \int_{\nu'_{sa}}^{1.25\nu'_{sa}} (\nu/\nu_{sa})^{-3/2} d\nu}{\int_{0.01\nu'_{sa}}^{\nu'_{sa}} (\nu/\nu_{sa})^{3/8} d\nu + \int_{\nu'_{sa}}^{500\nu'_{sa}} (\nu/\nu_{sa})^{-3/2} d\nu} \sim 1/6 \quad (\text{C.3})$$

which gives $\tau_{\gamma\gamma, MeV} \sim 1$ (from Equation C.2). It should be noted that here we make a conservative (although arbitrary) choice for the energy bin width $\Delta E_\gamma = \Gamma h(0.50\nu'_{sa})$ as η strictly corresponds to photons with energies very close to $\Gamma h\nu'_{sa}$.

The optical depth for pair annihilation is, $\tau_{e^-e^+} \sim (N_{e^-e^+}\sigma_{e^-e^+})/(4\pi R^2) \sim (3/8)(N_{e^-e^+}/N_{e, tot})(\tau_e/\beta'_e)$, where $N_{e^-e^+}$ is the total number of pairs in the jet and $\sigma_{e^-e^+} \sim (3/8)(\sigma_T/\beta'_e)$ is the pair annihilation cross section. Equating the pair production and annihilation rates at equilibrium

$$\frac{\sigma_{e^-e^+} N_{e^-e^+} \beta'_e c}{4\pi R^2} = \frac{\sigma_{\gamma\gamma, avg} N_{\gamma, MeV} c}{4\pi R^2} \quad (\text{C.4})$$

which gives

$$N_{e^-e^+} \sim 4.2N_{e,tot}\eta \sim 0.7N_{e,tot} \quad (\text{C.5})$$

for $\eta \sim 1/6$. Hence, the number of pairs $N_{e^-e^+}$ in the jet is always less than the total number of electrons $N_{e,tot}$.

We have not explored $\tau_{in} \lesssim 4$ while evaluating $N_{e^-e^+}$ as the photons at such low optical depths do not experience enough scatterings for Comptonization to modify the seed photon spectrum appreciably. Although f_ν can be larger by a factor of $\gtrsim 5$ for $1 \lesssim \tau_{in} \lesssim 2$, the number density of pairs and thus the pair annihilation optical depth, $\tau_{e^-e^+} \sim \sigma_{e^-e^+}n_{e^-e^+}$, is also larger by the same factor. This increases the probability of the additional pairs getting annihilated very quickly and the number of pairs is comparable to that obtained in Equation C.5. For larger values of $\tau_{in} \gtrsim 4$, $f_\nu \lesssim 10^{-5}$ which means that the number of pairs in the jet is even smaller. So, the effect of pairs can be ignored for the present work.

Bibliography

- [1] D. Band, J. Matteson, L. Ford, B. Schaefer, D. Palmer, B. Teegarden, T. Cline, M. Briggs, W. Paciesas, G. Pendleton, G. Fishman, C. Kouveliotou, C. Meegan, R. Wilson, and P. Lestrade. BATSE observations of gamma-ray burst spectra. I - Spectral diversity. *ApJ*, 413:281–292, August 1993.
- [2] A. Chhotray and D. Lazzati. Gamma-ray Burst Spectra and Spectral Correlations from Sub-photospheric Comptonization. *ApJ*, 802:132, April 2015.
- [3] Y. Kaneko, R. D. Preece, M. S. Briggs, W. S. Paciesas, C. A. Meegan, and D. L. Band. The Complete Spectral Catalog of Bright BATSE Gamma-Ray Bursts. *ApJS*, 166:298–340, September 2006.
- [4] R. D. Preece, M. S. Briggs, R. S. Mallozzi, G. N. Pendleton, W. S. Paciesas, and D. L. Band. The BATSE Gamma-Ray Burst Spectral Catalog. I. High Time Resolution Spectroscopy of Bright Bursts Using High Energy Resolution Data. *ApJS*, 126:19–36, January 2000.
- [5] M. J. Rees and P. Meszaros. Unsteady outflow models for cosmological gamma-ray bursts. *ApJL*, 430:L93–L96, August 1994.

- [6] T. Piran. The physics of gamma-ray bursts. *Reviews of Modern Physics*, 76:1143–1210, October 2004.
- [7] P. Kumar and B. Zhang. The physics of gamma-ray bursts and relativistic jets. *Physics Reports*, 561:1–109, February 2015.
- [8] B. Zhang and H. Yan. The Internal-collision-induced Magnetic Reconnection and Turbulence (ICMART) Model of Gamma-ray Bursts. *ApJ*, 726:90, January 2011.
- [9] P. Meszaros, M. J. Rees, and H. Papathanassiou. Spectral properties of blast-wave models of gamma-ray burst sources. *ApJ*, 432:181–193, September 1994.
- [10] T. Piran. Gamma-ray bursts and the fireball model. *Physics Reports*, 314:575–667, June 1999.
- [11] N. M. Lloyd and V. Petrosian. Synchrotron Radiation as the Source of Gamma-Ray Burst Spectra. *ApJ*, 543:722–732, November 2000.
- [12] S. Kobayashi, T. Piran, and R. Sari. Can Internal Shocks Produce the Variability in Gamma-Ray Bursts? *ApJ*, 490:92, November 1997.
- [13] D. Lazzati, G. Ghisellini, and A. Celotti. Constraints on the bulk Lorentz factor in the internal shock scenario for gamma-ray bursts. *MNRAS*, 309:L13–L17, October 1999.

- [14] P. Kumar. Gamma-Ray Burst Energetics. *ApJL*, 523:L113–L116, October 1999.
- [15] D. Guetta, M. Spada, and E. Waxman. Efficiency and Spectrum of Internal Gamma-Ray Burst Shocks. *ApJ*, 557:399–407, August 2001.
- [16] M. Kino, A. Mizuta, and S. Yamada. Hydrodynamic Effects in Internal Shock of Relativistic Outflows. *ApJ*, 611:1021–1032, August 2004.
- [17] B. Zhang, E. Liang, K. L. Page, D. Grupe, B.-B. Zhang, S. D. Barthelmy, D. N. Burrows, S. Campana, G. Chincarini, N. Gehrels, S. Kobayashi, P. Mészáros, A. Moretti, J. A. Nousek, P. T. O’Brien, J. P. Osborne, P. W. A. Roming, T. Sakamoto, P. Schady, and R. Willingale. GRB Radiative Efficiencies Derived from the Swift Data: GRBs versus XRFs, Long versus Short. *ApJ*, 655:989–1001, February 2007.
- [18] R. D. Preece, M. S. Briggs, R. S. Mallozzi, G. N. Pendleton, W. S. Paciesas, and D. L. Band. The Synchrotron Shock Model Confronts a “Line of Death” in the BATSE Gamma-Ray Burst Data. *ApJL*, 506:L23–L26, October 1998.
- [19] G. Ghirlanda, A. Celotti, and G. Ghisellini. Extremely hard GRB spectra prune down the forest of emission models. *A&A*, 406:879–892, August 2003.
- [20] P. Mészáros and M. J. Rees. Steep Slopes and Preferred Breaks in

Gamma-Ray Burst Spectra: The Role of Photospheres and Comptonization. *ApJ*, 530:292–298, February 2000.

- [21] M. J. Rees and P. Mészáros. Dissipative Photosphere Models of Gamma-Ray Bursts and X-Ray Flashes. *ApJ*, 628:847–852, August 2005.
- [22] D. Lazzati and M. C. Begelman. Non-thermal Emission from the Photospheres of Gamma-ray Burst Outflows. I. High-Frequency Tails. *ApJ*, 725:1137–1145, December 2010.
- [23] H. Ito, S. Nagataki, J. Matsumoto, S.-H. Lee, A. Tolstov, J. Mao, M. Dainotti, and A. Mizuta. Spectral and Polarization Properties of Photospheric Emission from Stratified Jets. *ApJ*, 789:159, July 2014.
- [24] R. Santana, P. Crumley, R. A. Hernández, and P. Kumar. Monte Carlo simulations of the photospheric process. *MNRAS*, 456:1049–1065, February 2016.
- [25] A. Pe’er, P. Mészáros, and M. J. Rees. The Observable Effects of a Photospheric Component on GRB and XRF Prompt Emission Spectrum. *ApJ*, 642:995–1003, May 2006.
- [26] D. Giannios. Prompt emission spectra from the photosphere of a GRB. *A&A*, 457:763–770, October 2006.
- [27] I. Vurm, A. M. Beloborodov, and J. Poutanen. Gamma-Ray Bursts from Magnetized Collisionally Heated Jets. *ApJ*, 738:77, September 2011.

- [28] A. Pe’er and F. Ryde. A Theory of Multicolor Blackbody Emission from Relativistically Expanding Plasmas. *ApJ*, 732:49, May 2011.
- [29] G. Ghisellini, G. Ghirlanda, L. Nava, and A. Celotti. GeV emission from gamma-ray bursts: a radiative fireball? *MNRAS*, 403:926–937, April 2010.
- [30] J. Granot, T. Piran, and R. Sari. The Synchrotron Spectrum of Fast Cooling Electrons Revisited. *ApJL*, 534:L163–L166, May 2000.
- [31] K. Toma, X.-F. Wu, and P. Mészáros. Photosphere-internal shock model of gamma-ray bursts: case studies of Fermi/LAT bursts. *MNRAS*, 415:1663–1680, August 2011.
- [32] D. Lazzati, B. J. Morsony, R. Margutti, and M. C. Begelman. Photospheric Emission as the Dominant Radiation Mechanism in Long-duration Gamma-Ray Bursts. *ApJ*, 765:103, March 2013.
- [33] C. Thompson. A Model of Gamma-Ray Bursts. *MNRAS*, 270:480, October 1994.
- [34] D. Giannios. The peak energy of dissipative gamma-ray burst photospheres. *MNRAS*, 422:3092–3098, June 2012.
- [35] D. Bégué, I. A. Siutsou, and G. V. Vereshchagin. Monte Carlo Simulations of the Photospheric Emission in Gamma-Ray Bursts. *ApJ*, 767:139, April 2013.

- [36] E. Liang, B. Zhang, F. Virgili, and Z. G. Dai. Low-Luminosity Gamma-Ray Bursts as a Unique Population: Luminosity Function, Local Rate, and Beaming Factor. *ApJ*, 662:1111–1118, June 2007.
- [37] D. Wanderman and T. Piran. The luminosity function and the rate of Swift’s gamma-ray bursts. *MNRAS*, 406:1944–1958, August 2010.
- [38] R.-R. Xue, Y.-Z. Fan, and D.-M. Wei. The initial Lorentz factors of fireballs inferred from the early X-ray data of SWIFT GRBs. *A&A*, 498:671–676, May 2009.
- [39] E.-W. Liang, S.-X. Yi, J. Zhang, H.-J. Lü, B.-B. Zhang, and B. Zhang. Constraining Gamma-ray Burst Initial Lorentz Factor with the Afterglow Onset Feature and Discovery of a Tight Γ_0 - E_{iso} Correlation. *ApJ*, 725:2209–2224, December 2010.
- [40] L. A. Pozdnyakov, I. M. Sobol, and R. A. Syunyaev. Comptonization and the shaping of X-ray source spectra - Monte Carlo calculations. *Astrophysics and Space Physics Reviews*, 2:189–331, 1983.
- [41] G. B. Rybicki and A. P. Lightman. *Radiative processes in astrophysics*. New York, Wiley-Interscience, 1979. 393 p.
- [42] R. Schlickeiser. *Cosmic Ray Astrophysics*. Cosmic ray astrophysics / Reinhard Schlickeiser, Astronomy and Astrophysics Library; Physics and Astronomy Online Library. Berlin: Springer. ISBN 3-540-66465-3, 2002, XV + 519 pp.

Vita

Mukul Bhattacharya was born in Bilaspur, India on 9 December 1993, the son of Goutam Bhattacharya and Shampa Bhattacharya. He grew up in Kharagpur, West Bengal and completed his schooling from Kendriya Vidyalaya, IIT, Kharagpur in May 2011. He received Bachelor of Science degree with Physics as major and Maths as minor concentration from the Indian Institute of Science (IISc), Bangalore in May 2015. After graduating among the first batch of undergraduate students from IISc with first-class honours and distinction, he joined as a graduate student in the Physics department at the University of Texas at Austin in August 2015.

Permanent address: 4210 Red River Street
Austin, Texas 78751

This dissertation was typeset with \LaTeX^\dagger by the author.

[†] \LaTeX is a document preparation system developed by Leslie Lamport as a special version of Donald Knuth's \TeX Program.